Geochemistry, Geophysics, Geosystems®

Key Points:

- Positive seismic radial anisotropy highlights the extent of rifting across the Sicily Channel
- The lithosphere beneath the Sicily Channel Rift Zone is thin, underlain by low seismic shear velocities and negative radial anisotropy
- Negative radial anisotropy in the upper mantle beneath the Sicily Channel suggests upwelling from slab-related poloidal flow

Supporting Information:

Supporting Information may be found in the online version of this article.

Correspondence to:

M. R. Agius,
matthew.agius@uniroma3.it

Shear-Velocity Structure and Dynamics Beneath the Sicily Channel and Surrounding Regions of the Central Mediterranean Inferred From Seismic Surface Waves

M. R. Agius[1,2] , **F. Magrini[3]** , **G. Diaferia[4]** , **E. D. Kästle[5]** , **F. Cammarano[1]** , **C. Faccenna[1,6]** , **F. Funiciello[1]**, and **M. van der Meijde[7]**

[1]Dipartimento di Scienze, Università Roma Tre, Rome, Italy, [2]Now at Dipartiment tal-Ġeoxjenza, L-Università ta' Malta, Msida, Malta, [3]Johannes Gutenberg-Universität Mainz, Mainz, Germany, [4]Istituto Nazionale di Geofisica e Vulcanologia, Rome, Italy, [5]Institute of Geological Sciences, Freie Universität Berlin, Berlin, Germany, [6]GFZ German Research Centre for Geosciences, Potsdam, Germany, [7]University of Twente, Enschede, The Netherlands

Abstract The evolution of the Sicily Channel Rift Zone (SCRZ) is thought to accommodate the regional tectonic stresses of the Calabrian subduction system. Much of the observations we have today are either limited to the surface or to the upper crust or deeper from regional seismic tomography, missing important details about the lithospheric structure and dynamics. It is unclear whether the rifting is passive from far-field extensional stresses or active from mantle upwelling beneath. We measure Rayleigh-and Love-wave phase velocities from ambient seismic noise and invert for 3-D shear-velocity and radial anisotropic models. Variations in crustal S-velocities coincide with topographic and tectonic features. The Tyrrhenian Sea has a ~10 km thin crust, followed by the SCRZ (~20 km). The thickest crust is beneath the Apennine-Maghrebian Mountains (~55 km). Areas experiencing extension and intraplate volcanism have positive crustal radial anisotropy ($V_{SH} > V_{SV}$); areas experiencing compression and subduction-related volcanism have negative anisotropy. The crustal anisotropy across the Channel shows the extent of the extension. Beneath the Tyrrhenian Sea, we find very low sub-Moho S-velocities. In contrast, the SCRZ has a thin mantle lithosphere underlain by a low-velocity zone. The lithosphere-asthenosphere boundary rises from 60 km depth beneath Tunisia to ~33 km beneath the SCRZ. Negative radial anisotropy in the upper mantle beneath the SCRZ is consistent with vertical mantle flow. We hypothesize a more active mantle upwelling beneath the rift than previously thought from an interplay between poloidal and toroidal fluxes related to the Calabrian slab, which in turn produces uplift at the surface and induces volcanism.

Plain Language Summary The Calabrian arc system in the central Mediterranean is undergoing multiple tectonic processes of subduction and lithospheric extension. Various models explain the evolution of this complex system but lack detail on the extension and rifting along the arc, particularly across the Sicily Channel. We use seismic data from 83 stations to image the seismic velocity of the lithosphere and asthenosphere below the region in high resolution. We map areas experiencing extension and compression and observe that these coincide with active seismicity and volcanism. We find that the Sicily Channel has a thinner than average crust, a thin mantle lithospheric lid, and is underlain by a low shear-velocity zone. Polarized shear velocities suggest mantle upwelling beneath the rift that produces uplift at the surface and induces volcanism. Our results provide new constraints on the evolution of the Calabrian slab and on the interplay between poloidal and toroidal fluxes of subduction zones.

1. Introduction

The central Mediterranean is made up of complex tectonic processes dominated by the northward slow convergence of the African continent with the Eurasian plate (Dewey et al., 1989) and the Calabrian subduction system retreating south-eastwards (Malinverno & Ryan, 1986). This area has been evolving for at least the last 30 My as the Calabrian subducting lithosphere rolled back from the west to the central Mediterranean (e.g., Carminati, Wortel, Spakman, et al., 1998; Carminati, Wortel, Meijer, et al., 1998; Faccenna et al., 2001; Goes et al., 2004; Carminati et al., 2012; Faccenna et al., 2014). Many studies have mapped in detail the seismic tectonic structures of the Calabrian arc, from the Apennines (e.g., Cimini & Marchetti, 2006; Kästle et al., 2018), down to Calabria (e.g., Barberi et al., 2004; Montuori et al., 2007; Neri et al., 2009; Orecchio et al., 2011; Totaro et al., 2014) and
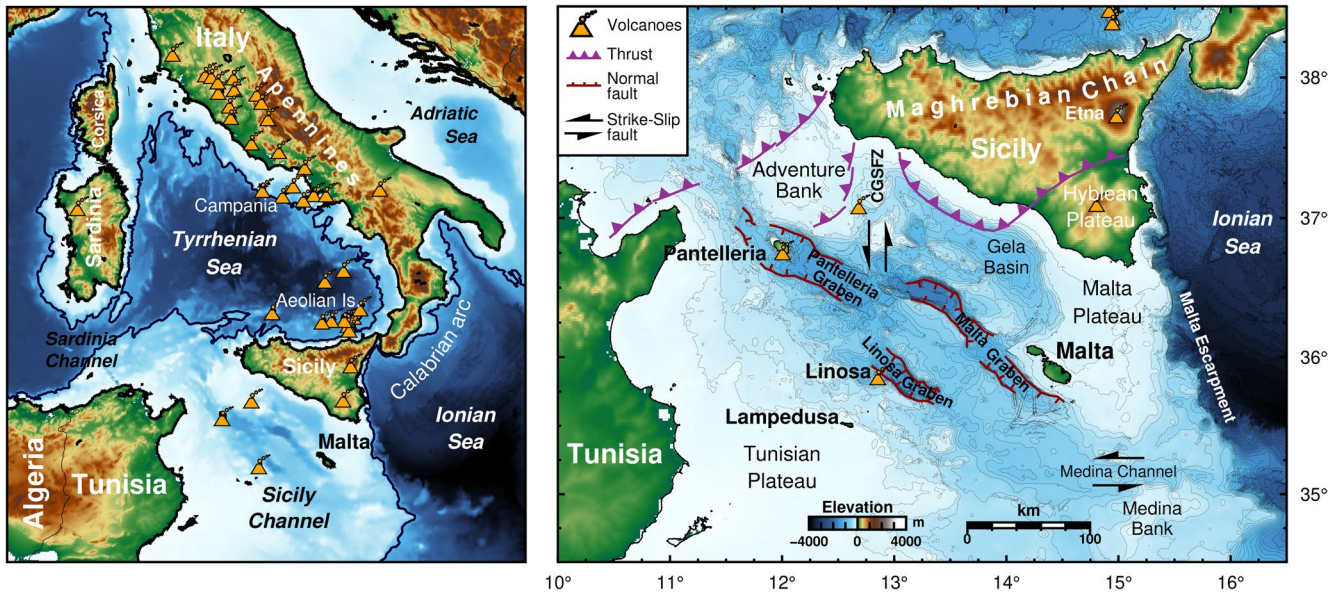
Figure 1. Regional maps of the study region. Left: Elevation map of the central Mediterranean. Black contour indicates the continental shelf. Right: Detailed map of the Sicily Channel highlighting the deep grabens that characterize the rift zone. Faint thin lines are contours at 100 m intervals. Purple fault lines are from Civile et al. (2018).

Sicily (e.g., Calò et al., 2013). The Sicily Channel Rift Zone (SCRZ), a ~500-km long offshore rift system, is located farther south of the arc between Sicily and Tunisia (Figure 1) (Finetti, 1985). The Sicily Channel accommodates the regional tectonic stresses through normal and dextral shear strike-slip faults that led to the formation of three deep grabens (Pantelleria, Linosa, and Malta) (Jongsma et al., 1985).

Much of the knowledge we have today on the Sicily Channel is either limited to surface observations such as seismic lines (e.g., Civile et al., 2008, 2010; Corti et al., 2006; Jongsma et al., 1985; Khomsi et al., 2016; Palano et al., 2020), earthquakes (e.g., Agius et al., 2020; Calò & Parisi, 2014), volcanism (e.g., Civetta et al., 1998; Parello et al., 2000), and plate motion (e.g., Anzidei et al., 2001; D'Agostino & Selvaggi, 2004; Serpelloni et al., 2013), or is from broader and deeper modeling from regional seismic tomography (e.g., Blom et al., 2020; El-Sharkawy et al., 2020; Lu et al., 2018; Piromallo & Morelli, 2003), potentially missing important details about the lithospheric structure of the Sicily Channel.

While there is a broad understanding of the Mediterranean mantle dynamics (Faccenna et al., 2014), many of the available seismic models are constrained by stations located on land, particularly along the Calabrian arc (e.g., Giacomuzzi et al., 2012; Lucente et al., 1999; Montuori et al., 2007). The lack of ocean-bottom seismometers limits the spatial resolution of the resulting models, mainly across the Tyrrhenian Sea (e.g., Greve et al., 2014; Magrini et al., 2022; Manu-Marfo et al., 2019) and the Sicily Channel (Kherchouche et al., 2020). Moreover, the Sicily Channel is at the periphery of large-scale Euro-Mediterranean wide seismic models and is therefore not well resolved (e.g., Blom et al., 2020; El-Sharkawy et al., 2020; Lu et al., 2018; Lucente et al., 2006; Marone et al., 2003; Piromallo & Morelli, 2003). Information such as the crustal and lithospheric thickness across the Sicily Channel is either incomplete (Calò et al., 2013; Manu-Marfo et al., 2019) or inconsistent with other geophysical features (Kherchouche et al., 2020), hindering our understanding of the dynamics of the SCRZ and thus of the complete Calabrian system.

The origin of the SCRZ is still debated. It has been proposed that the rift was formed by the pull of the deforming Calabria slab (Faccenna et al., 2005, 2007) or by delamination (Argnani, 1990) or mainly related to the strike-slip system (Boccaletti et al., 1987). It is also unclear whether the rifting of the SCRZ is passive or active. In the former, the driving forces of the rift are from far-field extensional stresses that stretch and thin the lithosphere while the asthenosphere passively fills in the new space created (e.g., Civile et al., 2010). In the latter, the lithosphere extension results from active mantle upwelling impinging on the base of the lithosphere leading, to the

opening of the rift (Huismans et al., 2001; Merle, 2011). Mapping the flow of the asthenosphere is, therefore, key to identifying the driving forces of the SCRZ.

Analog models (e.g., Funiciello et al., 2003, 2006; Kincaid & Griffiths, 2003) and numerical models (e.g., Piromallo et al., 2006) show that as a slab rollback, the lithosphere undergoes significant compression and extension (e.g., Magni et al., 2014). At the same time, the mantle experiences ductile flow where the upper mantle escapes from the front to the back of the arc (e.g., Faccenna et al., 2011; Lucente et al., 2006). Seismic shear-wave splitting studies confirm the presence of toroidal mantle flow beneath southern and western Sicily and the SCRZ (Civello & Margheriti, 2004); however, it remains unclear whether the flow is purely toroidal limited, to the horizontal (lateral) domain, or has a poloidal (vertical) component (e.g., Funiciello et al., 2006; Piromallo et al., 2006) that impinges on the base of the overlying lithosphere (e.g., Faccenna, Becker, Miller, et al., 2014; Faccenna et al., 2011).

This paper presents a new radially anisotropic, three-dimensional (3-D) shear-velocity model of the central Mediterranean region determined from ambient seismic noise recorded on old and newly available data sets. Particular focus is given to the Sicily Channel by maximizing the data coverage across its area. The model provides information about the structure of the crust, lithosphere, and mantle and about the patterns of stretching, compression, and flow. We interpret our results in combination with other geophysical properties to understand the crust and mantle dynamics beneath the Sicily Channel and their implications on the SCRZ.

2. Data and Methods

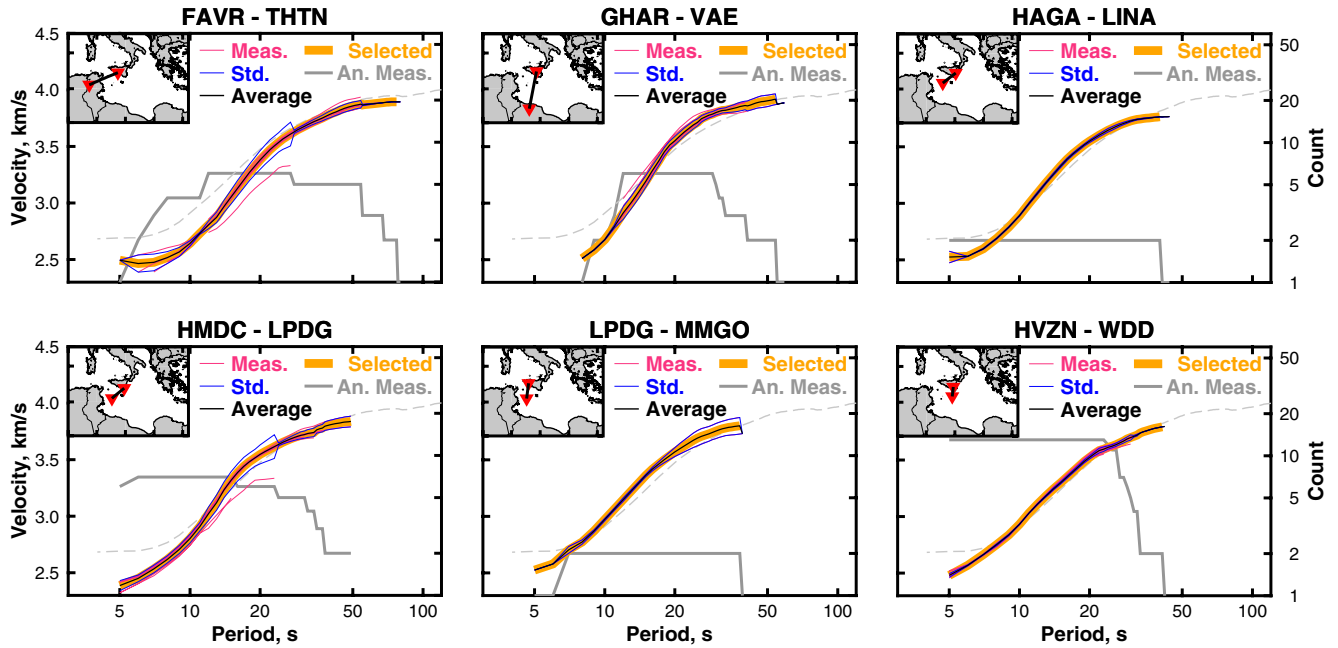### 2.1. Rayleigh- and Love-Wave Dispersion Curves

We use three-component continuous seismograms recorded on 83 stations located in the central Mediterranean. Many of these stations belong to different public and private networks and are part of permanent and temporary deployments that operated at different times. To ensure the best coverage across the Channel, we acquired data recorded between 1995 and 2018 and included station pairs that cross from the south of the Sicily Channel to eastern Libya, Greece, Albania, Central Italy, and Sardinia (LiSard seismic network, Magrini et al., 2019).

In a preliminary step, we removed instrument response, mean, and trend from the seismograms. We also band-pass filtered between 0.005 and 0.75 Hz and downsampled to 1 Hz. For each combination of station pairs for which simultaneous recordings are available, we then subdivide the preprocessed seismograms into overlapping (50%) one-hour-long time windows followed by spectral whitening (e.g., Bensen et al., 2007). We then cross-correlated the seismograms in the frequency domain. The resulting cross-correlations (one per time window) are then ensemble averaged to obtain a unique cross-spectrum. To prevent possible contamination by seismic phases different than the surface-wave fundamental modes (i.e., body waves and surface-wave overtones, Magrini & Boschi, 2021), we inverse Fourier transform each cross-spectrum and zero-pad in the time-domain at times corresponding to velocities smaller than two or greater than 5 km/s. We then Fourier transform the padded signals back to the frequency domain. This operation also contributes to smoothing the cross spectra and thus constraining the phase more robustly in the subsequent analysis (Magrini & Boschi, 2021; Magrini, Lauro, et al., 2022; Sadeghisorkhani et al., 2018).

We apply the automated algorithm of Kästle et al. (2016) to retrieve the dispersion curves from the cross-correlations. This algorithm relies on the fact that the cross-correlation of stochastic, horizontally propagating waves recorded at two stations approximately coincides with the zeroth-order Bessel function of the first kind, $J_0(\omega x/c(\omega))$ (Aki, 1957; Ekström et al., 2009), with ω denoting the angular frequency and x the interstation distance. The true, unknown phase velocity c can then be found by comparison of the zero crossings of the considered cross-spectrum with those of the associated Bessel function (e.g., Figure S1 in Supporting Information S1) (for technical details, refer to Kästle et al., 2016).

We calculate one dispersion curve for each year of simultaneous recordings on both stations. When multiple years of data are available, which for some stations pairs can exceed 10 years, we determine the average dispersion curve and the standard deviation. Individual outlier measurements that are more than one standard deviation away from the average are automatically discarded (e.g., Figure 2, HMDC-LPDG and HVZN-WDD, and the average dispersion curve is recomputed). The compiled interstation dispersion curves were then visually inspected and
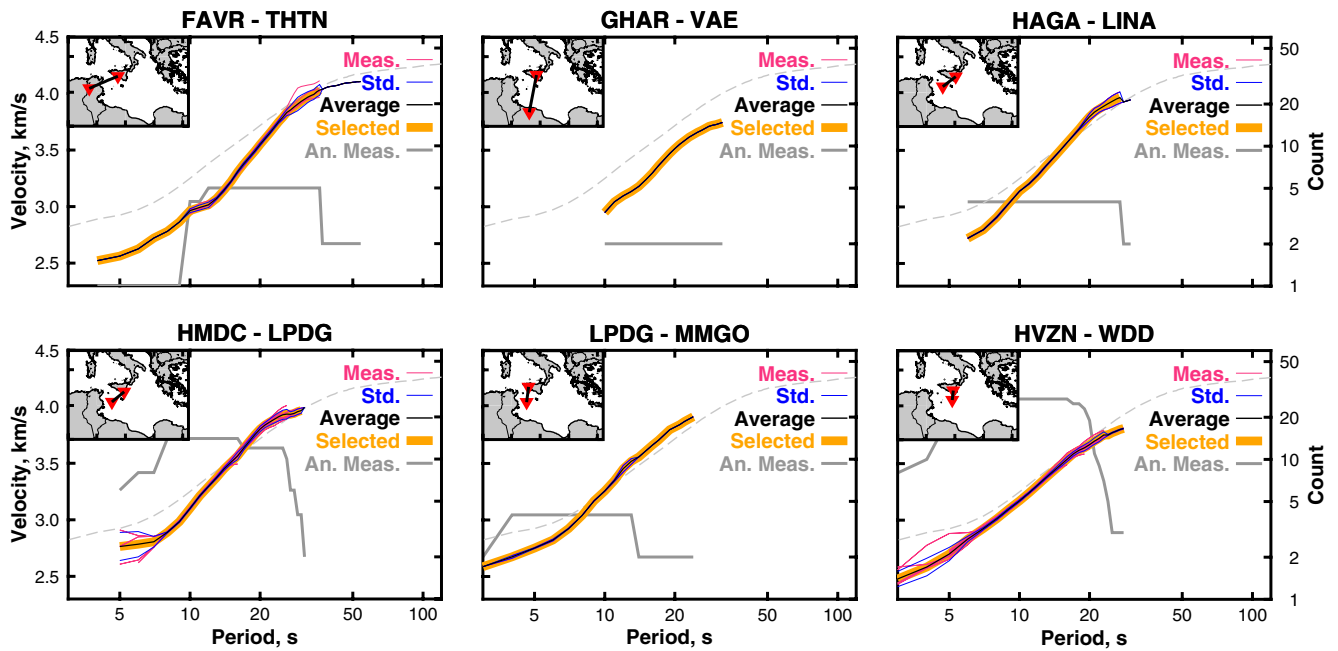
Figure 2. Example of smooth, broadband Rayleigh- (top) and Love-wave (bottom) dispersion curves. Each frame represents the phase-velocity measurement with period determined from station pairs indicated in the inset map. Dashed gray curve is the regional average, from all the measurements in this study. Individual pink curves are measurements from 1 year of data. Thin blue curves are one standard deviation. Black curve is the average dispersion curve. The selected average trimmed for further processing is highlighted in orange. Gray line shows the count of annual measurements.

trimmed to keep only the robust, smooth continuous parts of the curves for the final data set. Figure 2 shows examples of Rayleigh- and Love-wave dispersion curves from across the Sicily Channel.

Differences between individual dispersion curves are small, with larger standard deviations at the frequency ends investigated in this study. At the shorter periods (<8 s), such variability can be ascribed to the seasonality of the seismic ambient field (Yang & Ritzwoller, 2008; Gualtieri et al., 2021) and/or to the large ambiguity in phase (Magrini, Lauro, et al., 2022) associated with high density of zero-crossings (Figure S1 in Supporting Information S1). At longer periods (>30 s), larger uncertainties have been attributed to weaker ambient-noise signals and/or relatively low ratios between interstation distance and wavelength (Magrini, Diaferia, et al., 2019). Other issues could arise from stations with the wrong channel polarity, timing problems, or response problems (Weidle et al., 2013). Overall, from visual inspection of the dispersion curves, we find consistent annual measurements resulting in smooth station pair averages.

In total, we compile 1,731 Rayleigh- and 1,429 Love-wave interstation dispersion curves across the study region, with good coverage extending up to 100 and 50 s, respectively (Figures 3 and 4). At short periods (<20 s), interstation phase velocities across Africa and Italy are slower than those crossing the Tyrrhenian basin, indicating that the surface waves propagating along these paths are sampling continental crust. Some station pairs crossing the SCRZ have relatively faster velocities to the adjacent areas, suggesting crustal structural variability in the area. At longer periods (>30 s), phase velocities show less variability.

2.2. Phase-Velocity Maps

We invert the interstation dispersion curves to Rayleigh- and Love-wave phase-velocity maps at different periods. The method is based on ray theory and employs a spatially adaptive parametrization to accommodate strong heterogeneity across the path coverage (Boschi & Dziewonski, 1999; Lu et al., 2018). The resolution of the maps varies from a predefined $1.6° \times 1.6°$ coarse grid that is decreased iteratively to $0.2° \times 0.2°$ in the areas characterized by a high density of measurements (see Figures S2 and S3 in Supporting Information S1). The trade-off between the data fitting and the roughness of the model is regularized with a damping coefficient that is close to the maximum curvature of the "L-curve" (Hansen, 2001). No a-posteriori smoothing is applied to the maps shown in Figures 5 and 6. The linear inverse problem is solved via the iterative least-squares algorithm (Paige & Saunders, 1982).

Figures 5 and 6 show the output of the phase-velocity map inversions, which compare well to the raw data in Figures 3 and 4. The phase-velocity maps reveal structural variation within the crust and upper mantle. At short periods (<20 s), slow velocities follow contours of the continental shelves/blocks (Sardinia, northern Tunisia, and northern Sicily) in contrast to the faster velocities across the deep Tyrrhenian Sea. Slower velocities are located beneath the Apennine-Maghrebian chain. Interestingly, at periods >15 s, the grabens in the SCRZ have relatively faster velocities to the adjacent areas, suggestive of a thinner crust.

2.3. Resolution Test

To assess the resolution of the phase-velocity maps, we perform reconstruction tests at different surface-wave periods based on our Rayleigh and Love dispersion curves (Figures S4 and S5 in Supporting Information S1). We first create synthetic models characterized by checkerboard patterns of positive and negative phase-velocity anomalies. We then use these models to forward compute synthetic data (i.e., interstation phase velocities) through the SeisLib Python library (Magrini, Lauro, et al., 2022). The lateral extent of the anomalies is approximately equal to the average wavelength, and the velocity anomalies are ±10% with respect to the average velocity observed in the actual data at each period, similar to Magrini et al. (2022). We finally invert the synthetic data to retrieve the input model.

We find that data has good coverage offshore and onshore; across the Sicily Channel and the Tyrrhenian Sea, Sicily, Tunisia, Sardinia, and Southern Italy. The checkerboard test (Figures S4 and S5 in Supporting Information S1) establishes that the coverage for Rayleigh-wave data is suitable for a broad range of periods from 5 up to and exceeding 50 s, whereas Love-wave data is limited to <50 s, reflecting the fewer interstation data (Figures 3 and 4). These tests show that we have enough data coverage for our main study focus here, the Sicily Channel, potentially able to resolve small to large scale structures from the upper crust to the uppermost mantle.
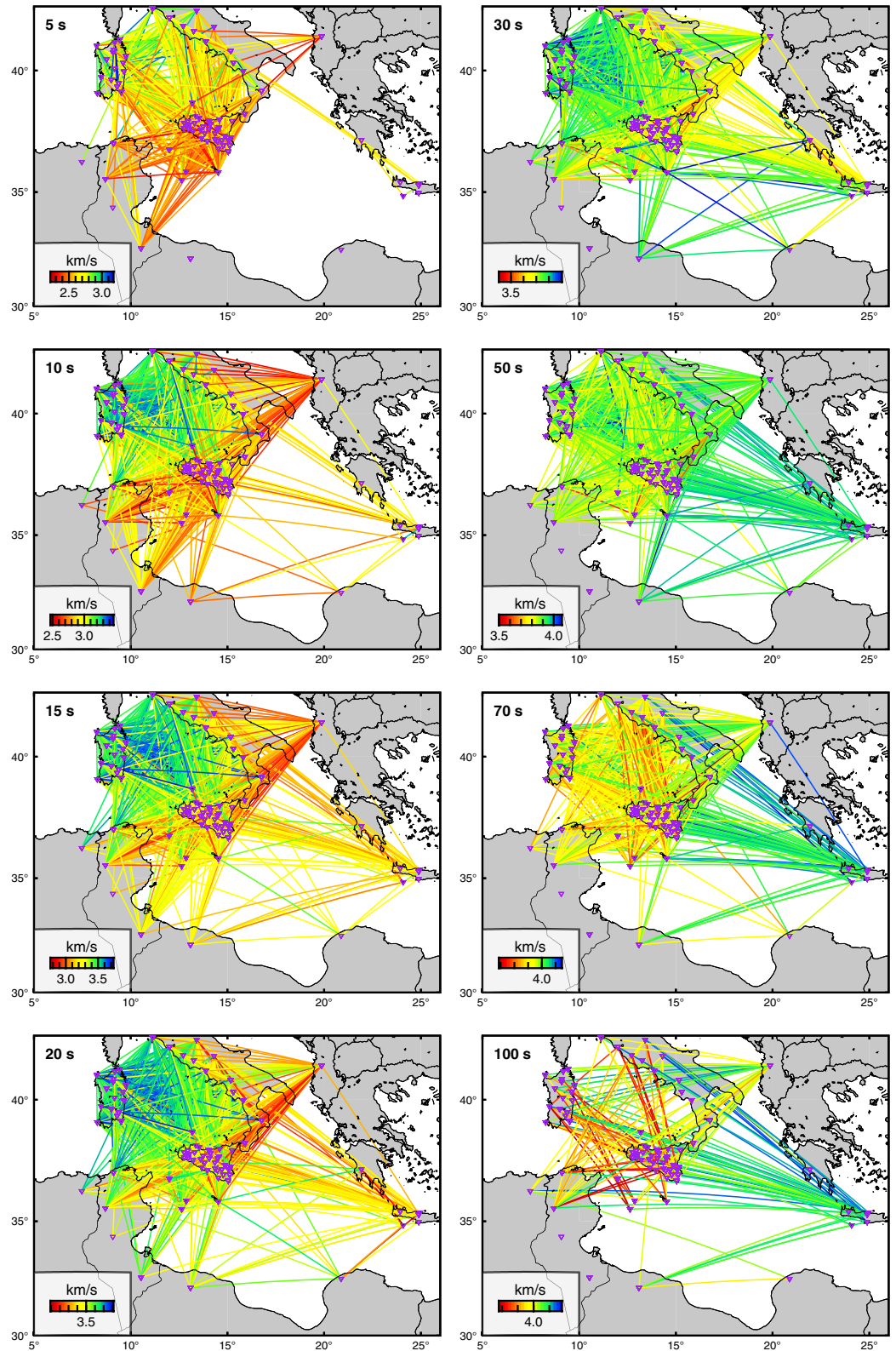
Figure 3. Seismic station distribution and interstation phase velocities for Rayleigh waves. Maps show the paths between station pairs (purple triangles) color-coded with phase velocity at the respective period indicated in the top left corner. Color-scale ticks have a value of 0.1.
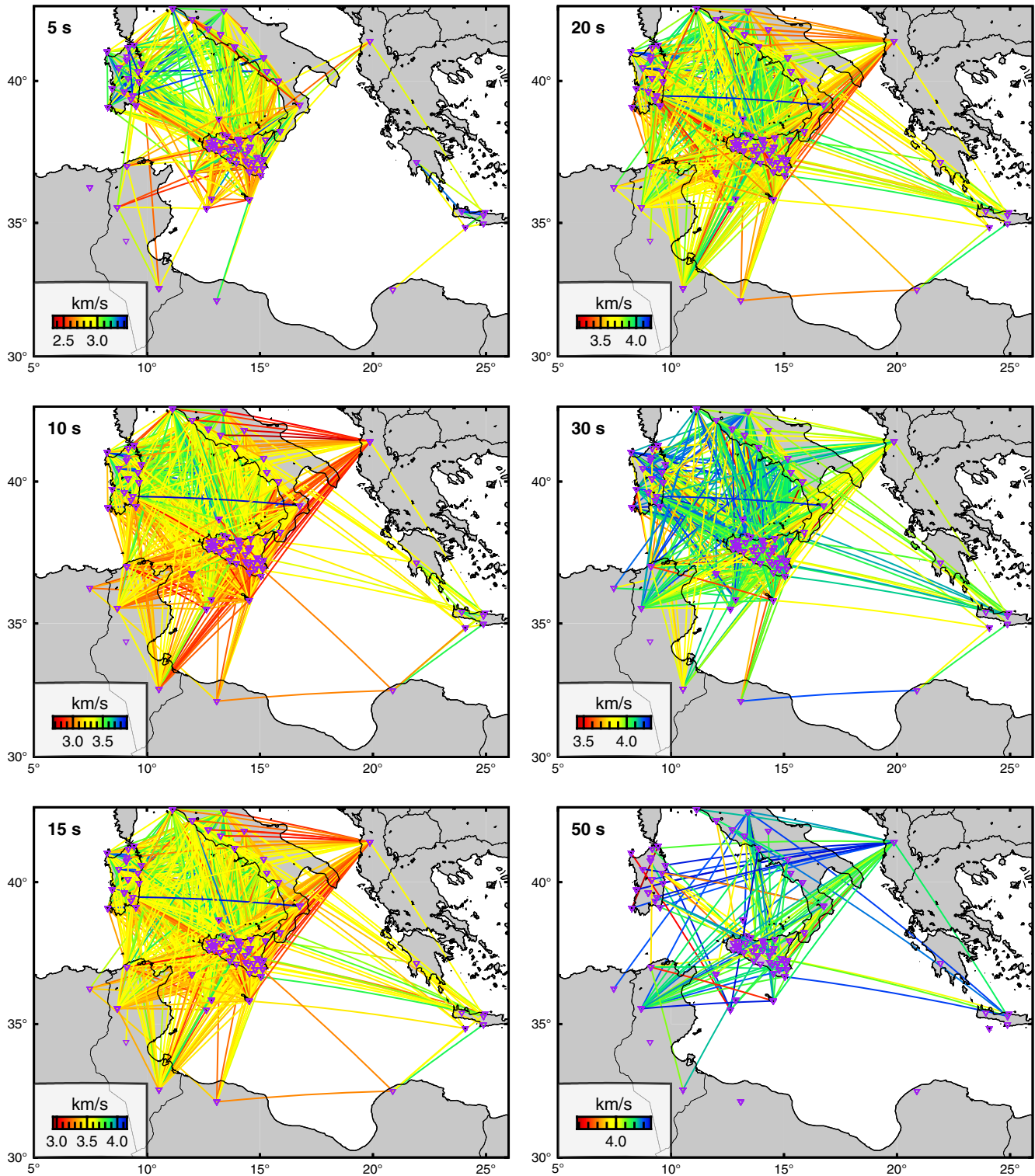
Figure 4. Seismic station distribution and interstation phase velocities for Love waves. Maps show the paths between station pairs (purple triangles) color-coded with phase velocity at the respective period indicated in the top left corner. Color-scale ticks have a value of 0.1.
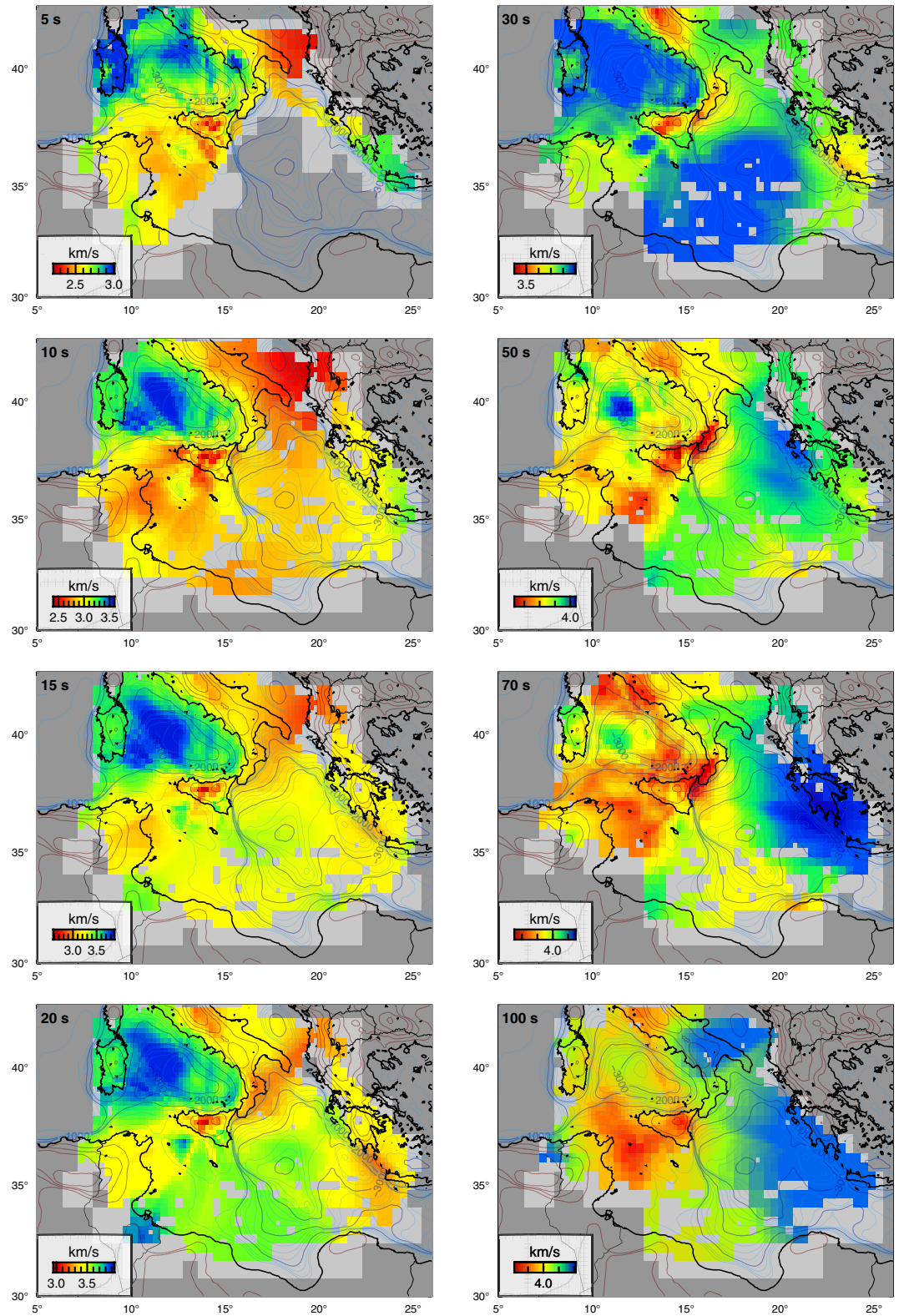
Figure 5. Rayleigh-wave phase-velocity maps. Phase-velocity maps at different periods are sensitive from the upper crust to the upper mantle. Red/blue shades show slower/faster velocities at the respective periods indicated in the top left corner. Color-scale ticks have a value of 0.1. Blue/red contours show the bathymetry/topography (ETOPO1, Amante & Eakins, 2009) at 250 m intervals with a median filter type of 100 km diameter (Wessel et al., 2019).
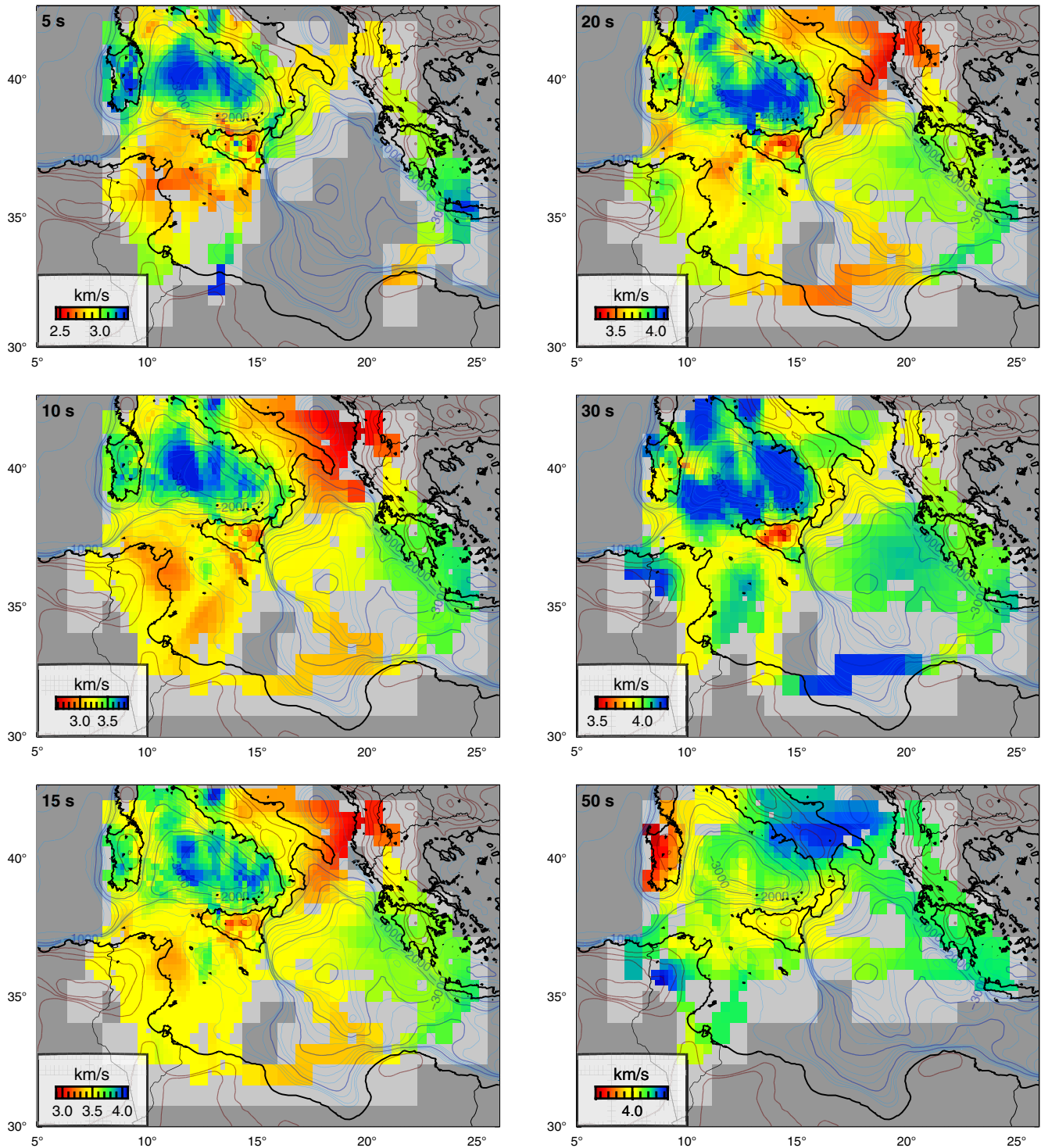
Figure 6. Love-wave phase-velocity maps. Phase-velocity maps at different periods sensitive from the upper crust to the upper mantle. Red/blue shades show slower/faster velocities at the respective periods indicated in the top left corner. Color-scale ticks have a value of 0.1. Blue/red contours show the bathymetry/topography (ETOPO1, Amante & Eakins, 2009) at 250 m intervals with a median filter type of 100 km diameter (Wessel et al., 2019).

2.4. Inversion for Shear Velocity

We invert the Rayleigh- and Love-wave dispersions jointly to obtain a 3-D isotropic shear velocity (V_S) model. We first interpolate the phase-velocity maps onto a $0.2° \times 0.2°$ grid for all periods. For each grid cell, a 1-D

Figure 7. Example of isotropic 1-D inverted shear-velocity profiles for a grid cell in the model (36.80°N, and 14.50°E) using the neighborhood algorithm. (a) Best fitting profiles color-coded by their respective misfit determined from the forward computed synthetic dispersion curves and the observed data (b and c). Black pr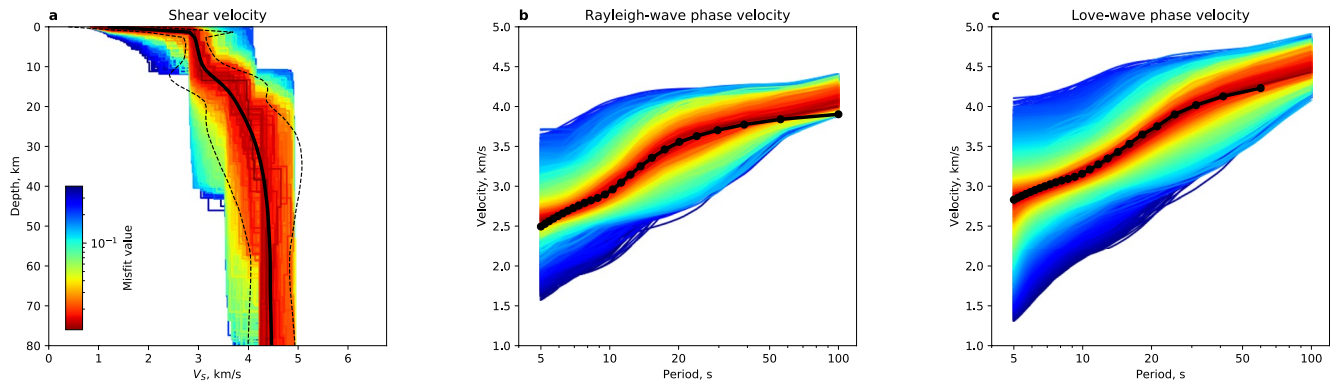ofile is the average of the best fitting models. The dashed line is one standard deviation. (b) Rayleigh-wave synthetic dispersion curves from profiles in (a) color-coded to represent misfit. Connected black dots represent the data points. (c) Same as (b) but for Love wave.

phase-velocity profile is extracted and inverted for the 1-D shear-velocity profile using the neighborhood algorithm (Sambridge, 1999a, 1999b; Wathelet, 2008; Wathelet et al., 2004). The inversion takes into account the different sensitives the two wave types have with depth. Figure S6 in Supporting Information S1 shows examples of the depth sensitivity the phase-velocity data has for different periods. The prior range for the 1-D model search is adapted from Kästle et al. (2018) and Magrini et al. (2022). It is made up of three layers for the crust and six layers for the mantle (each of which consisting of five sublayers) extending from the surface down to 400 km depth to also accommodate for deep structure that the data might be sensitive to. The thickness, V_S, P-wave velocity (V_P) and Poisson's ratio are free to vary within defined limits of each layer; for example, Poisson's ratio from 0.2 to 0.5 in the crust and 0.2–0.4 in the mantle, as similarly defined in Kästle et al. (2018) and Magrini et al. (2022). In principle, V_P has no influence on the Love-wave phase velocity and a minor influence on the Rayleigh-wave phase velocity (e.g., Aki & Richards, 2002). The density too has a very weak influence on the Rayleigh-wave phase-velocity dispersion and is therefore fixed in each layer (sediments: 2.4 g/cm³, upper crust: 2.75 g/cm³, lower crust: 2.9 g/cm³, 3.37 g/cm³ and higher in the mantle, same as in Kästle et al. (2018)). The algorithm is run through the software package Geopsy (Wathelet et al., 2020), which tries to minimize the misfit between the synthetic and the observed phase-velocity dispersion curves of Rayleigh and Love waves, jointly (Figure 7).

The neighborhood algorithm samples the parameter space by generating 8,000 random models. The best 200 models, that is, those associated with the lowest misfit values, are kept. In practice, the 1-D inversion is run in two steps: first to determine an estimate for the Mohorovičić (Moho) discontinuity depth and then using a Moho-adapted background model for a better starting model. Our preferred 3-D model is assembled by taking the average value of V_S as a function of depth for the 200 models at each location. We smooth the V_S profile to remove unrealistic velocity jumps stemming from different velocity discontinuities in the models (Kästle et al., 2018). Figures 8 and 9 show selected horizontal and vertical slices. In general, the V_S model shows similar characteristics as the Rayleigh- and Love-wave phase-velocity maps.

We also infer the crustal thickness by contouring the V_S at 4.0 km/s as a proxy for the crust-mantle discontinuity (Moho) (Figure 10). While the choice of an isosurface at 4 km/s is subjective, the V_S increase is typically considered as the signature of the Moho in global 1-D models (e.g., Dziewoński et al., 1981; Kennett & Engdahl, 1991). This value is similar to those used in other tomography studies (e.g., Kästle et al., 2018; Manu-Marfo et al., 2019). The effect of a lower or higher V_S can be seen in the vertical cross-sections (Figure 9), whereby a higher V_S would yield a thicker crust (deeper Moho) and vice versa.

The tomographic inversion method used here does not allow for radially anisotropic shear-velocity layers, that is, layers with different velocities for the horizontal and vertical polarized seismic wave propagation (Kästle et al., 2018; Wathelet, 2008). This may lead to a lower fit to the dispersion data in areas that have seismic radial anisotropy. We, therefore, invert for separate models of V_{SV} using only Rayleigh waves and of V_{SH} using only Love waves. We then determine the radial anisotropy $V_{SH} - V_{SV}/V_S$. We find that the differences between the models
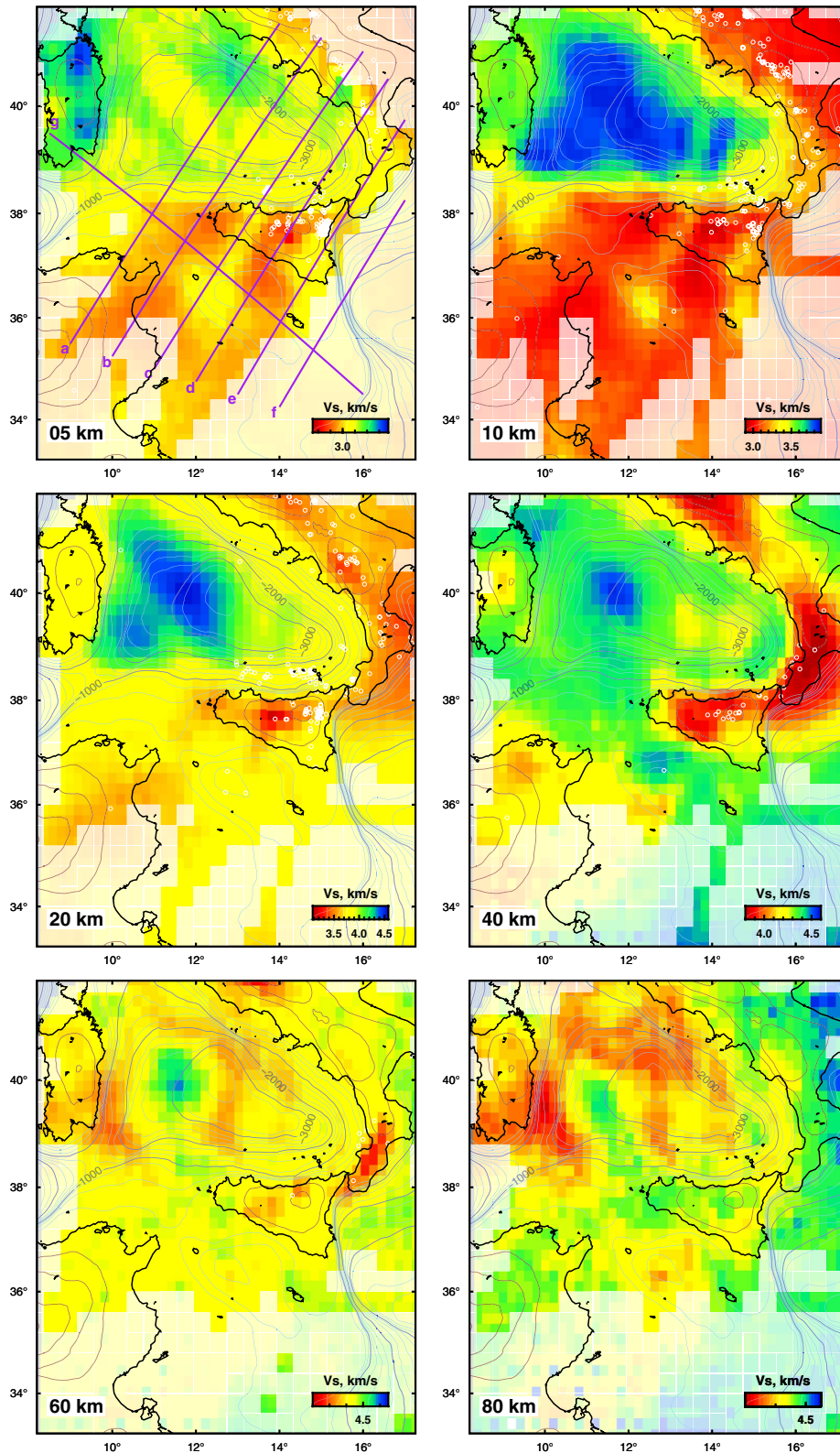
Figure 8. Maps of isotropic shear velocity. Red and blue shades show slow and fast absolute shear velocities, respectively, at different depths. Color-scale ticks have a value of 0.1. Light shaded areas are less resolved areas. White circles are earthquakes from the International Seismological Centre (2021) catalog from 1969 to 2020, magnitudes 1.2–7, and with an azimuthal gap less than 120° plotted at the respective depth ± half the depth difference between each slice. Blue/red contours show the bathymetry/topography (ETOPO1, Amante & Eakins, 2009) at 250 m intervals with a median filter of 100 km (Wessel et al., 2019).
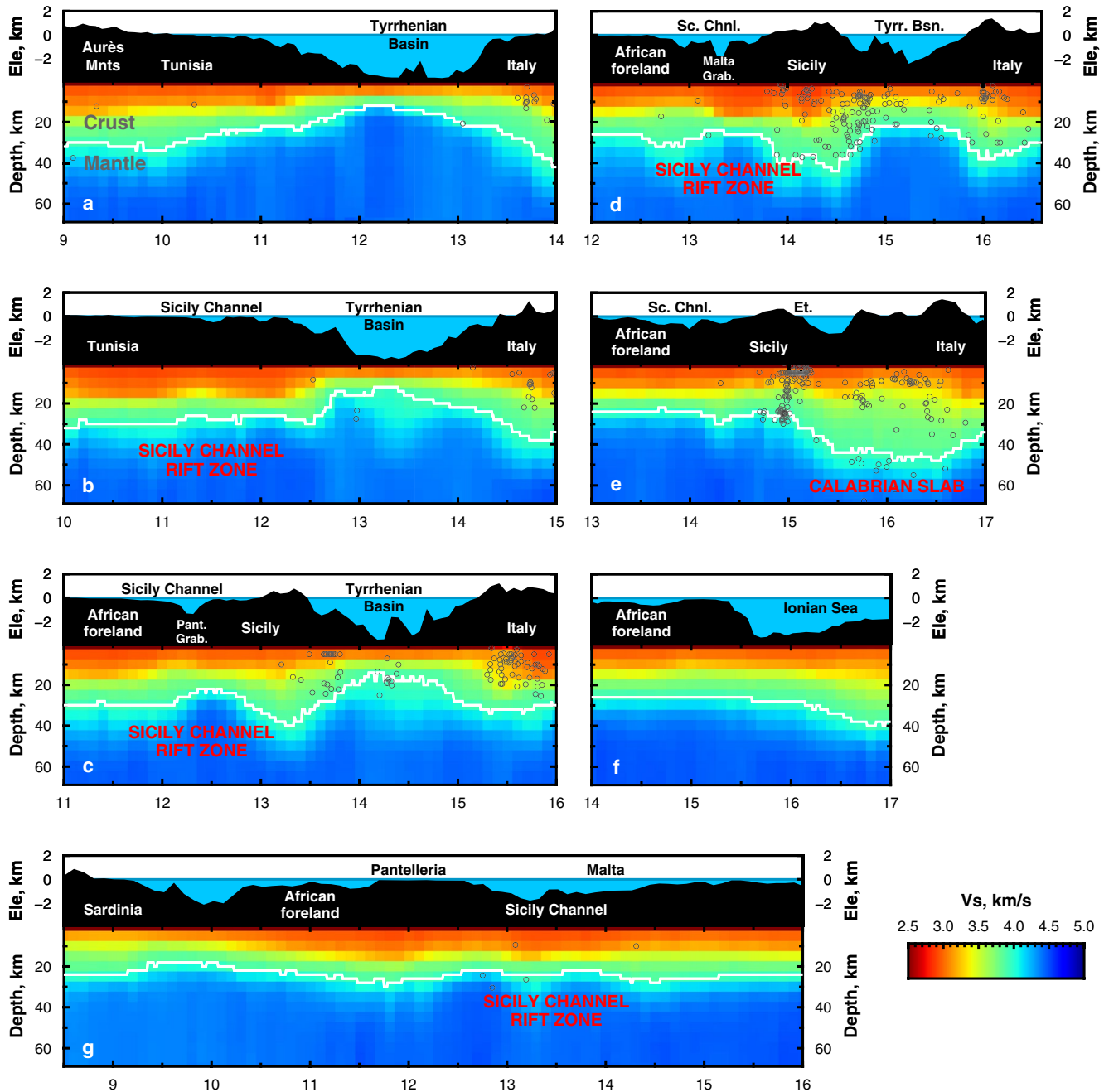
Figure 9. Vertical cross-sections of isotropic shear velocities. Red and blue shades show slow and fast absolute shear velocities, respectively. White line indicates the Moho depth inferred at 4 km/s. The elevation is shown on top. The location of the cross sections (a–g) are indicated in Figure 8. Black circles are earthquakes from the International Seismological Centre (2021) catalog from 1969 to 2020, magnitudes 1.2–7, and with an azimuthal gap less than 120° plotted along the respective profile with a ±0.3° width.

coincide with tectonic features likely linked to the V_S radial anisotropy, particularly in areas experiencing extension and compression (Figures 11 and 12). The shear-velocity, radial anisotropy, and crustal thickness models are available as Auxiliary Material.

Assessing the uncertainty of the seismic tomography model is generally difficult (e.g., Bodin et al., 2012; Rawlinson et al., 2014). We apply an independent method to verify the shear-velocity structure and particularly the amplitude of the radial anisotropy since this is not constrained in the 3-D model. We perform a joint Rayleigh- and Love-wave nonlinear, gradient-search inversion for V_S with depth that also takes into account the amplitude
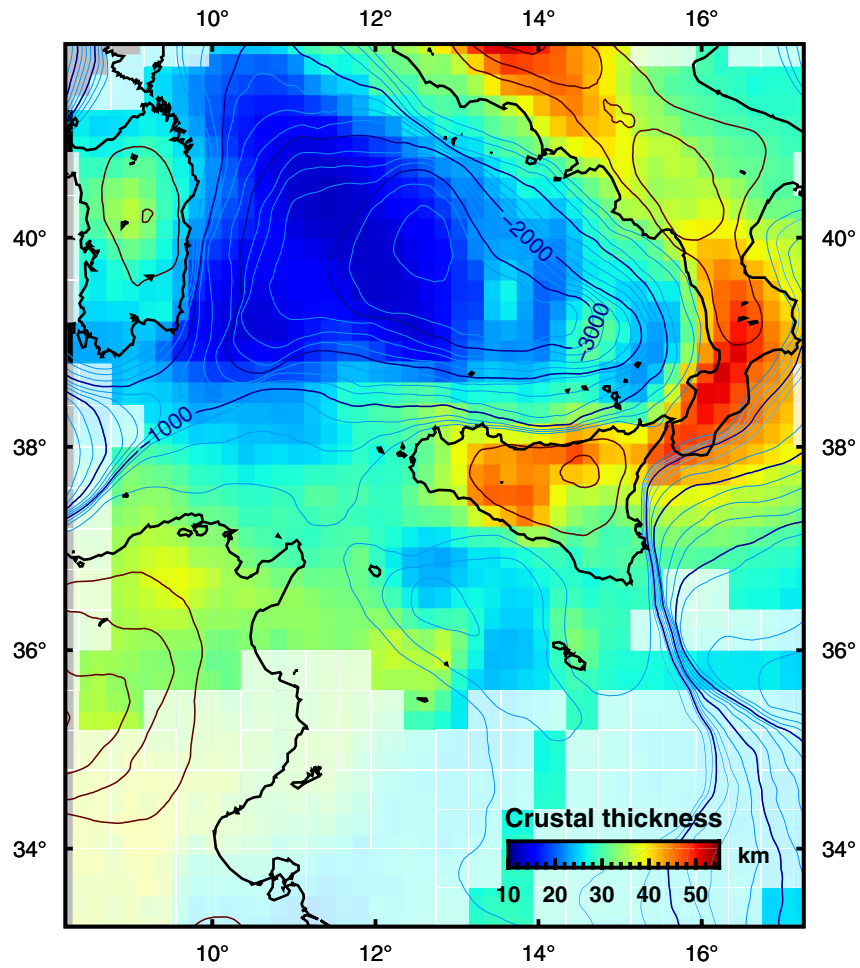
Figure 10. Map of crustal thickness. Blue and red shades indicate thin and thick crust, respectively, inferred from the shear-velocity model at 4 km/s. Red and blue contours show the smoothed topography and bathymetry (ETOPO1, Amante & Eakins, 2009), respectively, at 250 m intervals. Light shaded areas are less resolved areas.

of the anisotropy (Agius & Lebedev, 2013, 2014; Fullea et al., 2012; Vozar et al., 2014). We select five areas of interest (subregions) and average the dispersion curves of the Rayleigh and Love waves interstation pairs from within each region (Figure 13). Perturbations in the model are controlled by triangular-shaped basis functions, extending from the crust to the base of the upper mantle (e.g., Agius & Lebedev, 2014). The basis functions define the sensitivity depth range of two independent inversion parameters: the perturbation in isotropic-average V_S, and the amount of radial anisotropy. The depth of the Moho discontinuity is also an inversion parameter. Since the inverted models are nonunique, that is, slight variations in the models yield similar misfit (e.g., Agius & Lebedev, 2014; Fullea et al., 2012), we apply slight norm damping to avoid physically unrealistic models and acquire more robust models. We find that the shear velocities, crustal thicknesses, and radial anisotropy patterns in the subregions 1-D profiles (Figure 13) compare well with those in the 3-D model (e.g., Figures 9, 10 and 12).

3. Results

We present a new, isotropic 3-D shear-velocity model for the central Mediterranean based on manually selected dispersion curves (Figure 8). Strong velocity contrasts can be seen at different depths. At 5 km depth, eastern Sardinia has very fast upper crustal velocities (3.9 km/s), coherent with its Variscan crust (Magrini et al., 2019); the crust below the Tyrrhenian Sea has shear velocities in the range of 3.0–3.2 km/s, whereas Sicily and Tunisia have low velocities (<3.0 km/s). At 10 km depth, the V_S beneath the Tyrrhenian Sea increases to about 3.9 km/s. Sardinia has notable upper crustal velocities of ~3.6 km/s in contrast to Italy and the African foreland
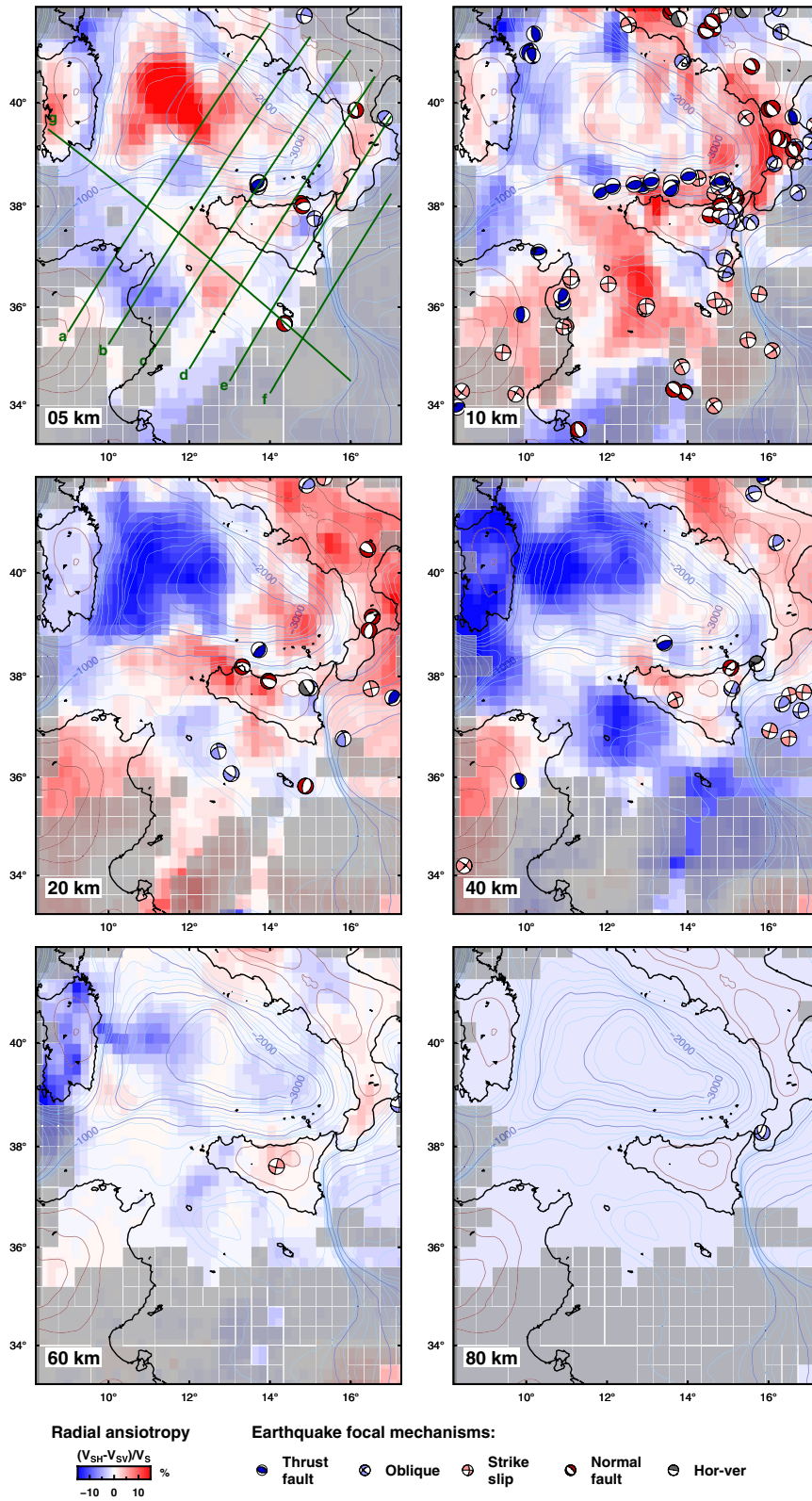
Figure 11.

(∼3.0 km/s), whereas the SCRZ has slightly higher velocities (∼3.3 km/s). These velocities compare well with velocities inferred from the sub-regional 1-D profiles (Figure 13). At 20 km depth, both Sardinia and Africa have similar lower crustal velocities (<4.0 km/s), whereas areas of higher topography, the Apennines and the Maghrebian Chain, have lower velocities. At 40 km depth, low crustal velocities (<4.0 km/s) are maintained beneath the mountain chains, whereas the other areas have typical upper mantle velocities. The center of the Tyrrhenian Sea and the Sicily Channel are marked by relatively higher V_S > 4.5 km/s. At deeper depths, the V_S structure shows no obvious pattern that can be related to the elevation above (Figure 8).

The thickness of the crust determined from the shear-velocity isosurface, overall, correlates with the elevation (Figure 10). The thinnest crust is found across the deep Tyrrhenian Sea (∼10 km), and thicker crust can be noted beneath mountains such as the Apennines—the thickest located beneath southeast Italy at the center of the Calabrian arc (∼55 km) (Figures 9 and 10). Sardinia has a relatively thin crust (<30 km), thicker beneath its mountains in the center. Sicily's crust varies from west to east, thick beneath the Maghrebian Chain (40–50 km) and thinner beneath the Hyblean Plateau (∼30 km), reflecting its geological history (e.g., Catalano et al., 1996). Tunisia and its foreland have a typical continental crustal thickness of about 30–35 km. In the Ionian Sea, the crust is <30 km thick, however, this is poorly constrained because of the lack of data coverage there (Figures S2–S5 in Supporting Information S1). Of main interest in this study is the SCRZ, where the deeper parts of the grabens are marked by a thin crust of ∼20 km in contrast to other areas in the Sicily Channel (Figure 9, cross-sections: a–d). The crustal thicknesses from the 3-D model are confirmed with the results of the subregions 1-D profiles (Figure 13).

The radial anisotropy model shows patterns of positive and negative anisotropy across the region and at different depths that agree with the seismicity of the area. We plot the earthquake focal mechanisms from the European-Mediterranean Regional CMT (Figures 11 and 12, Pondrelli, 2002) and find that the mechanisms coincide with the different signs of anisotropy. For example, at 5 km depth, earthquakes representing thrust faults are located in areas of negative radial anisotropy, whereas earthquakes from normal faults are in areas of positive anisotropy (Figure 11). Similar patterns are observed at 10 km and other depth slices. Reasons for disagreements between focal mechanism and radial anisotropy vary and are discussed below. The radial anisotropy of the Tyrrhenian Sea and the SCRZ change from positive at <10 km depth to negative for depths >20 km, in the mantle (Figure 11), in agreement with the subregions 1-D inversion models (Figure 13). The subregions 1-D models also confirm that the radial anisotropy can be as strong as 10%.

4. Discussion

We compare our shear-velocity model with local geophysical studies such as seismic receiver functions, seismic reflection, seismic tomography, gravity, and magnetism, and also compare it with regional-scale models. We also examine the positive and negative radial anisotropy patterns inferred from the model and compare them with patterns of volcanism, plate velocities from Ground Positioning Systems (GPS), and earthquake focal mechanisms. The good agreement between the different studies gives us confidence in the model, especially in areas previously not investigated. Finally, we discuss the crustal and mantle dynamics of the region, particularly of the SCRZ.

4.1. Shear Velocity Structure of the Central Mediterranean

The Sicily Channel is often at the periphery of many large-scale Euro-Mediterranean wide seismic models (e.g., Blom et al., 2020; Boschi et al., 2009; El-Sharkawy et al., 2020; Lu et al., 2018; Magrini et al., 2022; Marone et al., 2003; Piromallo & Morelli, 1997, 2003; Spakman, 1990; Spakman et al., 1993) or of regional-scale Italy-focused models (e.g., Alessandrini et al., 1995; Barberi et al., 2004; Cimini, 1999; Cimini & Gori, 1997; Cimini & Marchetti, 2006; Giacomuzzi et al., 2012; Greve et al., 2014; Li et al., 2010; Lucente et al., 1999;

Figure 11. Maps of radial anisotropy. Red and blue shades show positive and negative percentages of radially polarized shear velocities, respectively, at different depths. Gray shaded areas are less resolved areas. Beach balls are earthquake solutions from the European-Mediterranean Regional Centroid-Moment Tensors (CMT) website (https://doi.org/10.13127/rcmt/euromed) (Pondrelli, 2002) between 1997 and 2020 and magnitudes from 3.5 to 7, color-coded to represent different focal mechanisms derived from fault plane solutions on the basis of P- and T-axis plunge angles (Lindenfeld et al., 2012), and plotted at the respective depth ± half the depth difference between each slice. Blue/red contours show the bathymetry/topography (ETOPO1, Amante & Eakins, 2009) at 250 m intervals with a median filter of 100 km (Wessel et al., 2019).
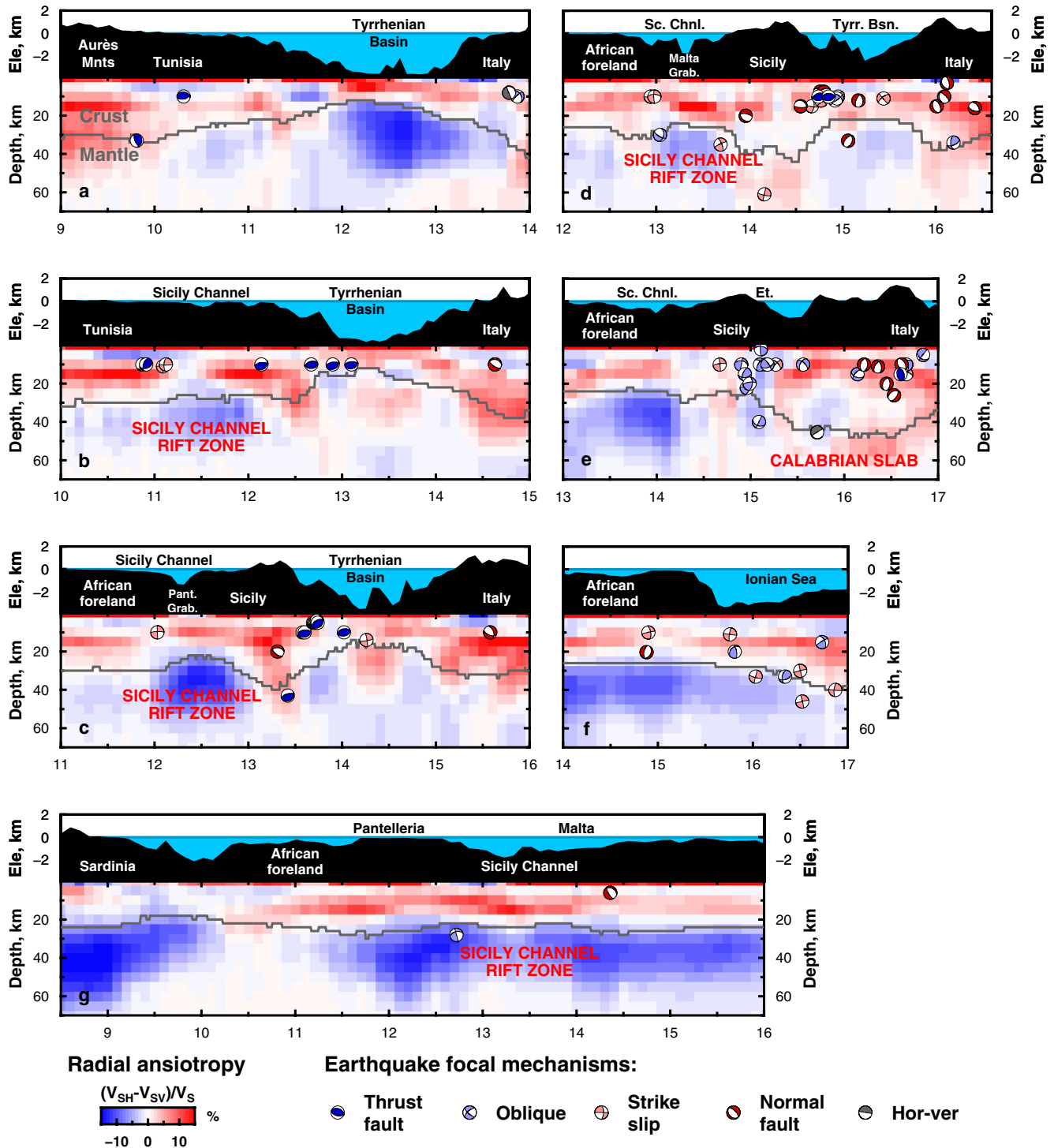
Figure 12. Vertical cross-sections of radial anisotropy. Red and blue shades show positive and negative percentages of radially polarized shear velocities, respectively. The location of the cross sections (a–g) are indicated in Figure 11. The elevation is shown on top. Beach balls are earthquake solutions from the European-Mediterranean Regional Centroid-Moment Tensors website (https://doi.org/10.13127/rcmt/euromed) (Pondrelli, 2002) between 1997 and 2020 and magnitudes from 3.5 to 7, color-coded to represent different focal mechanisms derived from fault plane solutions on the basis of P- and T-axis plunge angles (Lindenfeld et al., 2012), plotted as viewed on a map and plotted along the respective profile with a ±0.3° width. Gray line indicates the Moho depth inferred at 4 km/s.
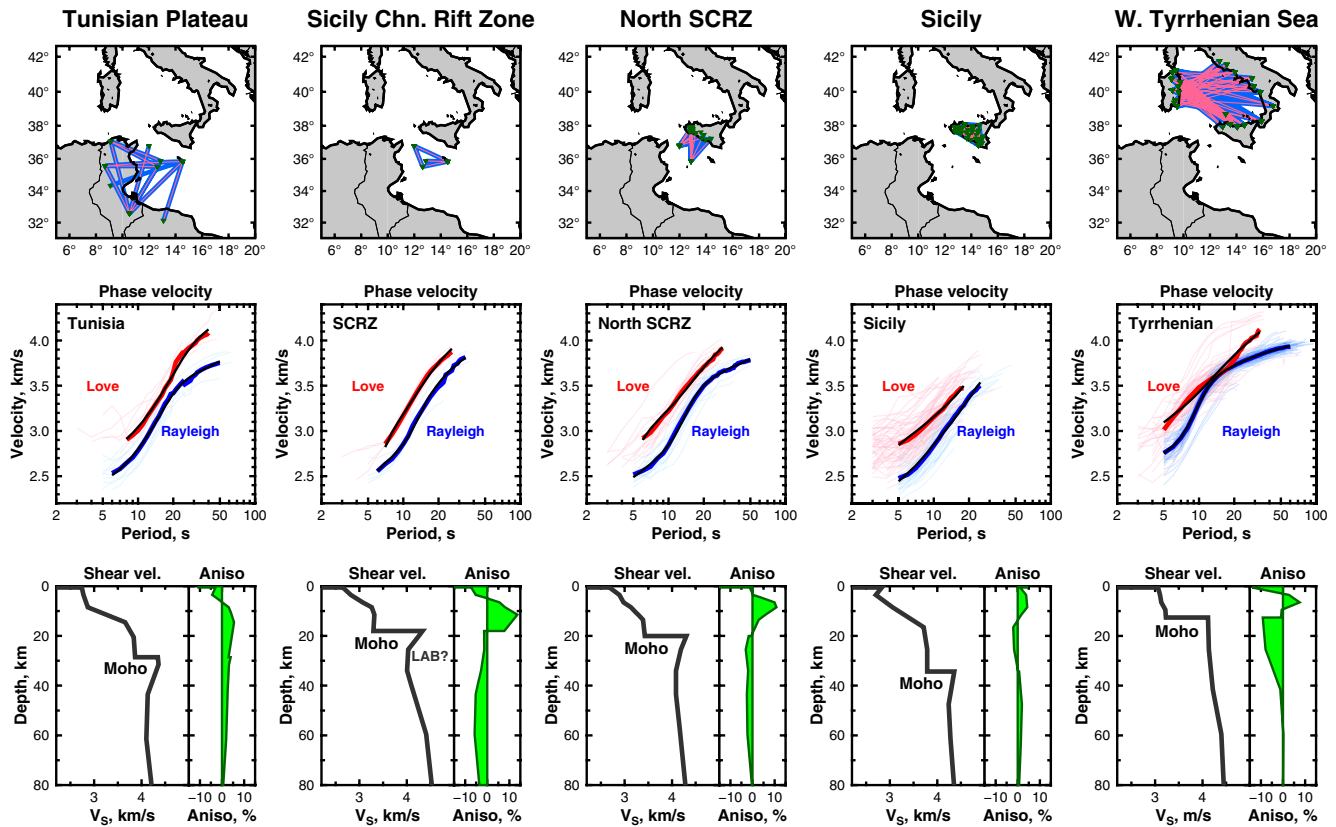
Figure 13. 1-D radially anisotropic shear-speed profiles for five subregions. Top: Map of interstation pairs used for Rayleigh- (blue) and Love-wave (pink) average phase-velocity measurements. Middle: Rayleigh- and Love-wave dispersion curves. Pale curves are from individual measurements corresponding to the interstation pairs on top, bold curves are the subregional averages. Black curves are the synthetic dispersion curves determined from the 1-D profile (bottom). Bottom: 1-D radially anisotropic V_S profile obtained in a nonlinear, gradient-search joint inversion of Rayleigh- and Love-wave dispersion. Green profiles show the radial anisotropy with depth. Moho marks the crust-mantle discontinuity.

Manu-Marfo et al., 2019; Neri et al., 2009; Orecchio et al., 2011; Pontevivo & Panza, 2002; Scarfì et al., 2018; Sgroi, Polonia, et al., 2021), with only a few studies providing coverage across the Channel (Calò et al., 2013; Kherchouche et al., 2020). While these models use different data and techniques that naturally lead to different resolutions, it remains unclear which are the robust features. For example, travel time tomography shows low *P*-wave velocities across the Tyrrhenian Sea in the upper 40 km (Scarfì et al., 2018), whereas surface-wave studies show high shear velocities (Manu-Marfo et al., 2019). Across the Sicily Channel, Scarfì et al. (2018) and Calò et al. (2013) show fast velocities in the upper 30 km in contrast to the slow velocities in Kherchouche et al. (2020), also inferred from seismic surface-wave data. Moreover, these models tend to have little correlation with the bathymetry and seismicity across the Sicily Channel, probably due to poor resolution in the area.

Our new model has the advantage of encompassing the entire central Mediterranean by using all the publicly available seismic data from northern Africa (Algeria, Tunisia, and Libya) paired with the corresponding stations that operated during the same time. Additionally, the model includes the private seismic network LiSard on Sardinia, which significantly improves the lateral coverage across the Tyrrhenian Sea, the Sicily Channel, and neighboring areas. Much of the shallow V_S structures coincide with topographic and tectonic features of the region: slow under the high-elevation mountain chains, fast beneath the deep sea (Figure 8). In general, our model agrees with the shear velocities and crustal structure of the recent study of Manu-Marfo et al. (2019), although we find more pronounced features in the upper 20 km, such as beneath Sardinia (in agreement with Magrini et al., 2019), across the Tyrrhenian Sea, and across the Italian peninsula coinciding with elevation (Figure 8). In the upper mantle, we agree with the recent tomographic model of Magrini et al. (2022), particularly across the Tyrrhenian Sea. Unlike here, Magrini et al. (2022) used dispersion data inferred from teleseismic earthquakes and seismic ambient noise.

The additionally performed 1-D inversions of the subregions provide better constrain on the vertical changes in the profiles. Unlike in tomography, where each cell in the grid is inferred from an average of phase velocities crossing several tens of interstation paths (some paths crossing hundreds of kilometers, Figures 3 and 4, Figures S2 and S3 in Supporting Information S1), here we use only the paths from within the specified area, providing a more direct relationship between the data and the structure. The subregion 1-D inversions have no *apriori* constraint on the smoothness of the lateral variations (i.e., no roughness damping) introduced in the tomography. Additionally, the 1-D inversions parameterization fits better the Rayleigh- and Love-wave data by allowing for radial anisotropy. The subregional profiles show a sharp discontinuity at the Moho, and in the case of the Sicily Channel, the Moho discontinuity is underlain by a shallow low-velocity zone (LVZ) in the mantle, suggesting a region of transition from the lithosphere to a hot asthenosphere (Figure 13).

Defining the exact depth of the lithosphere-asthenosphere boundary (LAB) seismically is difficult, particularly if the V_S decreases smoothly with depth (Eaton et al., 2009). The LAB, here defined to coincide with the lowest V_S in the upper mantle, is at about 60 km depth beneath the Tunisian Plateau, rises to ∼33 km beneath the SCRZ, and deepens again toward Sicily. The lithospheric mantle lid beneath the SCRZ is thus about 10 km thick. The rising of the LAB from Tunisia to the Sicily Channel has also been inferred from gravity modeling farther northwest of the Channel (Cella et al., 1998). Studies on the LAB beneath eastern Sicily from joint inversion of P and S receiver functions give a LAB depth of 63 km (Monna et al., 2019) and 70–90 ± 15 km from S receiver functions (Miller & Piana Agostinetti, 2011), with the latter using a fixed 1-D model for migration (iasp91, Kennett & Engdahl, 1991).

The thinnest lithospheric mantle lid is reportedly beneath the Tyrrhenian Sea, where it is less than 10 km inferred from the joint inversion of Rayleigh-wave group and phase velocities (Panza et al., 2003; Pontevivo & Panza, 2002). Manu-Marfo et al. (2019) report LAB depths at 40 km, while Greve et al. (2014) report deeper LAB depths at 70 km depth. Our models do not show a distinct LVZ beneath the Tyrrhenian Sea but low sub-Moho velocities that increase monotonically with depth.

Differences between models can be attributed to different factors, for example, different data coverage (i.e., we use a newly available data set from Sardinia), the use of phase velocities rather than group velocities, and/or differences arising from strong seismic anisotropic properties in the rocks identified in our models but that are unrepresented in others—all elements likely to produce slightly different tomographic models. The presence of very deep waters, not accounted for in this study, can also introduce a bias in the inversion of Rayleigh waves for V_S, albeit this issue does not seem to be relevant for the Sicily Channel, where the bathymetry is relatively shallow (Zhou et al., 2016).

At 60–80 km depth, a ring-shaped low-velocity feature surrounding a fast velocity anomaly appears beneath the Tyrrhenian Sea (Figure 8), similar to that observed by Greve et al. (2014) and Magrini et al. (2022) at the same depth. These low shear velocities may be explained by the presence of water in the Tyrrhenian mantle (Karato & Jung, 1998; Karato, 2012) since significant hydrous fluids are expectedly released from the dehydration of the subducting lithosphere (e.g., Faccenda et al., 2012). The fast velocity in the center of the circular feature may be, on the other hand, the signature of a dehydrated upper mantle (Karato & Jung, 1998).

The Sicily Channel is characterized by a relatively low V_S anomaly at 80 km depth (Figure 8). In spite of the limited resolution of our data at this depth, this is in agreement with the recent regional surface-wave studies of El-Sharkawy et al. (2020). In the absence of subducted lithosphere, the slower velocities are attributed to higher temperatures, possibly contributing to the high heat flow observed in this area (e.g., Vedova et al., 1995). High temperatures are also likely to lower the viscosity of the rocks, which, in turn, facilitate mantle circulation. The role mantle flow has on the regional dynamics is discussed in Section 4.4.

4.2. Crustal Thickness

The crustal thickness inferred here compares well with those from high-resolution localized studies. For example, our thickness estimates across Italy have an excellent agreement with the Moho depth inferred from receiver functions (Piana Agostinetti & Amato, 2009), with both results showing distinctively thick crust beneath the Apennines and the Calabrian arc with Moho depths around 50 km (Figure 10). Similarly for southern Sardinia, where receiver functions show a Moho depth of 29 km depth (van der Meijde et al., 2003). Another excellent agreement is with profiles from deep seismic sounding crossing from Tunisia to Sardinia, where beneath Tunisia

(Tell Mountain area) the crust is about 35–40 km thick, thinning to 20 km toward the north beneath the Sardinia Channel, and to 30 km thick beneath the center of Sardinia (Morelli & Nicolich, 1990). A similar good agreement is found with the model of Di Stefano et al. (2011) constrained by receiver functions and controlled source seismology, where the crust thins from 30 km beneath Sardinia to 10 km beneath the Tyrrhenian Sea.

With no seismic stations located in the Tyrrhenian Sea, and with the techniques used here, resolving for localized ultra-thin crust (<10 km, e.g., Prada et al., 2015) is difficult primarily because the dispersion data are representative of the long interstation paths crossing the sea in this area. Thus, areas that have experienced strong crustal heterogeneity in the southeastern Tyrrhenian Sea from the Calabrian arc subduction (Prada et al., 2020) are likely to be weakly resolved here. Furthermore, the 4.0 km/s isocontour that we use as a Moho proxy does not necessarily coincide with the true Moho in all regions, especially in areas where the model shows a gradual increase in V_S from the crust to mantle or where the shear velocity structure is perturbed by the presence of fluids or by temperature anomalies.

In general, the inferred Moho depth is further validated by comparison with the seismicity pattern. Most earthquakes occur within the crust, as expected, with some earthquakes located close to the Moho contour (Figure 9). Sub-Moho earthquakes are mainly located beneath the Tyrrhenian Sea and associated with the Calabrian slab. Our model agrees with European-wide crustal models too (Grad et al., 2009; Molinari & Morelli, 2011).

Sicily is characterized by a thick crust (>40 km) to the west and north areas along the Maghrebian mountain chain, and with a continental type crustal thickness to the southeast beneath the Hyblean Plateau (Figure 10). This contrast is also observed from gravity and magnetic models (Milano et al., 2020). Receiver functions from Piana Agostinetti and Amato (2009) confirm the Moho depth beneath the Hyblean Plateau of about 30 km. Across the Channel, close to Pantelleria, estimates for the crustal thickness from seismic reflection show the Moho discontinuity at 17 km beneath the graben deepening rapidly to 25 km southwest of the graben (Civile et al., 2008), coinciding with our area of thin crust east of Pantelleria in Figure 10.

The crustal thickness inferred from other surface-wave studies for the Tyrrhenian Sea and neighboring areas (Greve et al., 2014; Manu-Marfo et al., 2019) in general show similar patterns to our model but with less agreement to the local studies mentioned above. Moreover, in these studies, the Sicily Channel is located at the periphery of their models. The consistency of our crustal model with measurements from previous studies give us confidence on the robustness of our 3-D V_S model, especially across the Sicily Channel, where we have very good coverage thanks to the seismic stations located on both sides of the Channel and on the islands in the center of the SCRZ (e.g., Figures S4 and S5 in Supporting Information S1). Beneath the grabens, the crust is relatively thinner by 10–15 km when compared to the surrounding areas and coincide with the deep sea and active volcanoes (Figures 1 and 10). To the north-west of the Channel, no significant crustal thinning is observed, which suggests that Sicily is connected to the African foreland and that a Sicilian Block microplate has not fully developed (Cello, 1987; Jongsma et al., 1985).

4.3. Present-Day Crustal Extension Across the Sicily Channel Rift Zone

4.3.1. Seismicity and Earthquake Focal Mechanisms

We show the regional seismicity by plotting the earthquake hypocenters superimposed on the shear-velocity cross-sections in Figures 8 and 9 in order to identify areas of tectonic activity. Most of the seismic activity is located along the Calabrian arc, and the majority of the earthquakes occur in the upper 10–20 km of the crust, above the Moho discontinuity. Sub-crustal earthquakes occur on the Calabrian slab, down to the mantle transition zone (e.g., Chiarabba et al., 2005; Presti et al., 2013).

The Sicily Channel too is characterized by seismicity (e.g., Agius et al., 2020; Calò & Parisi, 2014; Kherchouche et al., 2020; Palano, 2014; Palano et al., 2020); however, many of the earthquake hypocenters are poorly constrained because (a) earthquake waveforms originating from the center of the SCRZ are strongly attenuated, often making it challenging to pick the P wave necessary for earthquake location algorithms (e.g., Agius et al., 2020), and (b) because of large station azimuthal gaps (station gaps around the earthquake location). The Sicily Channel is surrounded by four different national networks that operated at different time periods. Small-magnitude earthquakes were usually only located by the Italian National Seismic Network using stations from Sicily on the northern side of the Channel (e.g., D'Alessandro et al., 2011). We select earthquakes that have good station coverage,

with an azimuthal gap less than 120° (International Seismological Centre, 2021), to automatically eliminate potentially uncertain earthquake hypocenters (particularly the depth parameter) outside seismic networks. We prefer this approach because discriminating earthquake locations on the basis of travel time errors, although it is a good statistical assessment, might be biased if most stations are far away from the source (Bondár et al., 2004). We do not find any well-constrained deep earthquakes within the SCRZ (>30 km), with the deepest earthquake located close to the Moho discontinuity. Considering the rifting environment of the Sicily Channel, deep mantle earthquakes >60 km (e.g., Kherchouche et al., 2020; Palano et al., 2020) are unlikely because they are not observed in other rift systems such as the East African Rift (Lindenfeld & Rümpker, 2011; Lindenfeld et al., 2012; Yang & Chen, 2010). The lack of deep earthquakes is also supported by the better-constrained CMT (Figures 11 and 12).

Earthquake fault plane solutions from the CMT provide important information on the fault mechanism at depth. Each earthquake CMT (Pondrelli, 2002) is color-coded to represent one of five kinematic categories: thrust, strike, normal, oblique (i.e., thrust-strike or normal-strike), and horizontal-vertical, following a classification scheme similar to Frohlich (1992) based on the plunge angles of P- and T-axis (e.g., Lindenfeld et al., 2012; Sgroi, Barberi, & Marchetti, 2021). Distinct mechanisms at different areas of the central Mediterranean and at different depths can be noted in Figures 11 and 12.

While earthquake CMT gives accurate, high-resolution information on the local geodynamics at depth, seismic anisotropy from tomography can offer extended information on the regional deformation pattern. Radial seismic anisotropy (i.e., the difference between horizontally and vertically polarized shear speeds) is generally associated with large, finite strain within the Earth that develops a preferred alignment of the anisotropic minerals. In the shallow crust (∼5 km), anisotropy is generally explained by shape-preferred orientation, caused by tectonic stresses that align microcracks, melts, and foliations to a specific direction (e.g., Crampin & Chastin, 2003). For example, the 1D profiles (Figure 13) show that the shallow crust has negative radial anisotropy, probably a result of such cracks in the crust that are typically oriented sub-vertically. In the lower crust, crystallographic-preferred orientation is usually related to mineral alignments due to their deformation (e.g., Shapiro et al., 2004; Weiss et al., 1999). In the mantle, anisotropy is associated with the lattice-preferred orientation (LPO) of the dominant mineral olivine, which aligns parallel to the direction of mantle flow (Zhang & Karato, 1995). The polarity of the radial seismic anisotropy (positive or negative) may thus provide added information on the type of mechanism that influenced the fabric within the crust or mantle. For example, crustal extensional processes as a result of stretching or flattening align the minerals horizontally, which in turn yields to faster shear speeds in the horizontal domain and therefore positive radial seismic anisotropy ($V_{SH} > V_{SV}$) (e.g., Agius & Lebedev, 2014). Seismic anisotropy may represent active deformation or past deformation that has left an anisotropic fabric frozen in the rocks. For example, in the recent study of Alder et al. (2021), they attribute positive radial anisotropy observed in the lower crust of the Apennines (also observed here) to ductile horizontal flow in response to the recent and present-day extension in the region.

We compare the earthquake mechanisms, which represent the current deformation processes, with the inferred patterns of the radial seismic anisotropy. The overall agreement is significant: normal or strike-slip fault earthquakes are in areas of positive anisotropy, and thrust or oblique earthquakes are located in areas of negative anisotropy ($V_{SH} < V_{SV}$). For example, at 10 km depth, thrust fault earthquakes north of Sardinia are in an area of negative anisotropy (Figure 11). The region of Calabria is characterized by normal faults (positive anisotropy) and oblique faults on the eastern coast (negative anisotropy). Thrust (reverse) faults are located offshore northern Sicily as a result of the compression from the subduction process taking place there at the boundary between positive and negative radial anisotropy. Our results complement the recent model of Alder et al. (2021), which shows strong positive radial anisotropy (10%–20%) in the lower crust of the Apennines. The Apennines, too, are characterized by normal faults and earthquakes (Trippetta et al., 2019).

On Sicily, a narrow column of negative radial anisotropy is identified beneath Mt. Etna, likely capturing the vertical ascent of magma from the upper mantle to the surface, coinciding with oblique earthquake focal mechanisms that cut through the entire crust (Figures 12e and 9e). The Hyblean Plateau has oblique earthquakes and negative radial anisotropy. Across the Sicily Channel, shallow earthquakes are predominately strike-slip in an area of positive radial anisotropy. At 20 km depth, however, anisotropy switches to negative and earthquakes have an oblique mechanism (Figure 11).

Different earthquake mechanisms overlapping on the horizontal cross-section at 10 km depth (Figure 11) may be a result of the default depth set in the earthquake location algorithm (e.g., Pondrelli et al., 2002) or may be a result of complex fault processes occurring within narrow areas or depth ranges. In the latter case, earthquakes are better viewed from the vertical cross-sections. A change in the radial anisotropy polarity and the earthquake focal mechanism close to 10 km depth can be seen beneath Tunisia (Figures 12a–12c).

4.3.2. Volcanism and GPS Vectors

We compare the shallow radial anisotropy from our data with volcanism and velocity vectors from GPS. We find that the positive and negative anisotropy coincide with intraplate and subduction-related volcanism, respectively (Figure 14a, Faccenna et al., 2005). The center of the Tyrrhenian Sea is characterized by strong positive radial anisotropy and intraplate volcanism, probably a consequence of lithospheric stretching from the Calabrian back-arc extension in the last 10 Ma (Faccenna et al., 2001). Areas that are close to past and ongoing subduction, such as Campania and the Aeolian Islands, have subduction-related volcanism and negative radial anisotropy. Similarly, the Sicily Channel is characterized by recent intraplate volcanism and shallow positive radial anisotropy.

GPS can provide information on the orientation and rate of deformation that are taking place today. Figure 14b shows that the direction of the horizontal vectors located on Tunisia and Sicily with respect to Eurasia as a fixed reference point is north-northwest with a velocity of about 4 mm/yr parallel to Africa's plate movement (McClusky et al., 2003). On a closer inspection, one notes a slight eastern (clockwise) shift in the vector direction between stations on the Tunisian platform, for example, LAMP with those on Sicily (Figure 14b) (Anzidei et al., 2001; Bahrouni et al., 2020; Civile et al., 2008; Corti et al., 2006; D'Agostino & Selvaggi, 2004; Devoti et al., 2011; Serpelloni et al., 2005). The difference between the vectors is often attributed to the rifting process (e.g., Jongsma et al., 1985; Reuther et al., 1993; Serpelloni et al., 2005). We show the differential movement between the GPS stations on LAMP with those of eastern Sicily, similar to Corti et al. (2006) (Figure 14b, red arrows plotted in the middle between the respective stations). The resultant vector is oriented SW–NE with velocity differences of about 1.5 mm/yr. The orientation is perpendicular to the normal faults that characterizes the SCRZ (Jongsma et al., 1985; Reuther et al., 1993) and is parallel to the extension component of the principal axes from earthquakes located in the southeastern areas of the Sicily Channel (Figures 14b and 14c). While GPS shows that extension is taking place there at the surface, the earthquakes moment tensor indicates that the extensional process is also taking place at the respective depth of the earthquakes (e.g., Agius & Lebedev, 2017). The extension is also supported by the positive radial anisotropy mapped between Pantelleria, LAMP, and MALT (Figures 11 and 14), which thus highlights the lateral extent of the extension across the Sicily Channel at the respective depth.

A similar comparison between the GPS station on Malta (MALT) with the stations on southeastern Sicily yields null velocity differences, meaning that MALT is tectonically well connected with the Hyblean Plateau, also in agreement with the lack of positive radial anisotropy there. And, in another comparison for the northwestern end of the Sicily Channel where we compare GPS stations located on northern Tunisia (Bahrouni et al., 2020) and Pantelleria with stations located on Sicily, the differential vectors are oriented NW–SE on top of Adventure Bank with magnitudes <2 mm/yr (Figure S7 in Supporting Information S1). This area is also characterized by positive radial anisotropy, and is located between two thrust faults. We do not interpret these observations further due to the lack of evidence, for example, seismicity (Figure 14c). A comparison between station PZIN with station TUNI yields a resultant null vector suggesting that the two are coupled together (Figure S7 in Supporting Information S1).

We also look into patterns of radial anisotropy with the vertical velocity vectors from GPS. Under isostasy, areas undergoing extensions are potentially subsiding by a few millimeters a year, while areas experiencing collision (compression) or vertical mantle flow will be rising. We plot recent GPS vertical measurements that have a data time span of at least 3 years to reduce potential influence from seasonal hydrological variations (Figure S8 in Supporting Information S1, Serpelloni et al., 2013). We do not plot data from stations located on top of volcanic complexes because these are likely to undergo strong volcanic-related variability (e.g., Campania, the Aeolian Islands, Western Sardinia, and the Sicily Channel). We find that the negative and positive vertical velocities correlate with areas of positive and negative radial anisotropy, respectively; correlate positively in the first 10 km and then a negative at 20–40 km, and no correlation below (Figure S8 in Supporting Information S1). A detailed
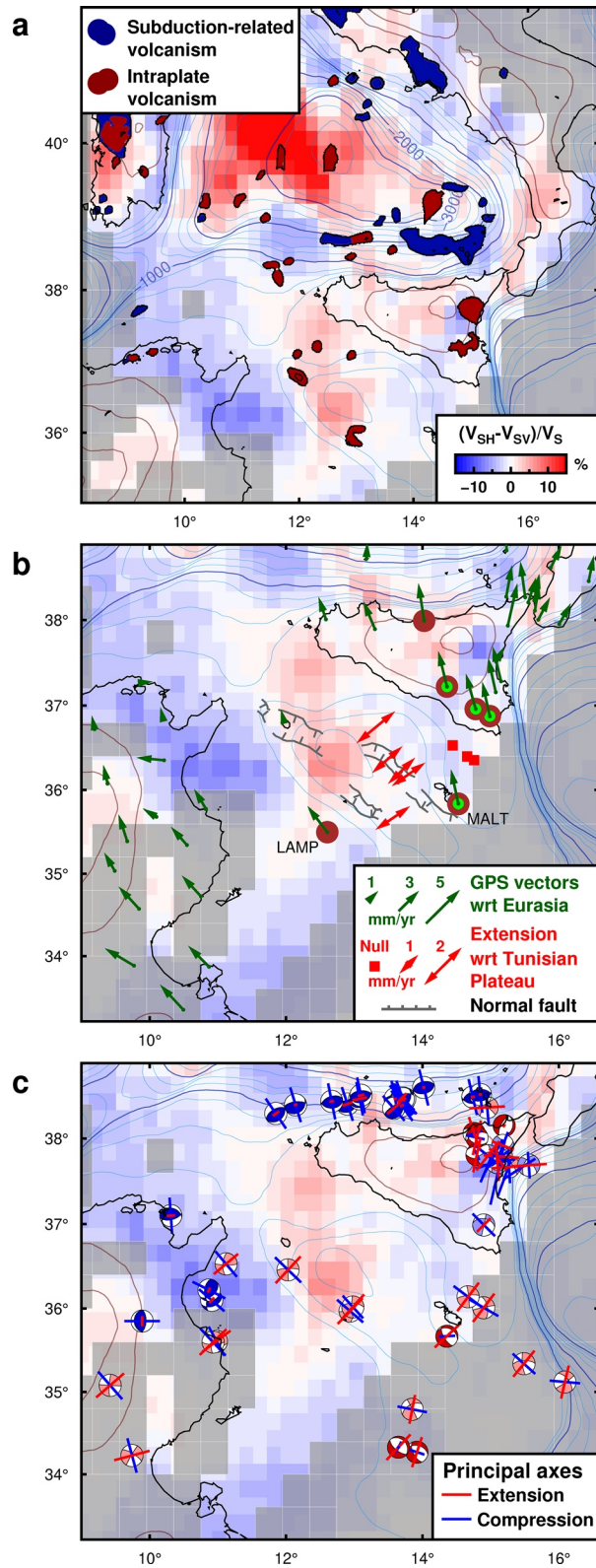
Figure 14.

investigation on the possible relationship between radial anisotropy and the GPS vectors, and also the role mantle dynamics may have on surface deformation remains desirable.

The agreement of the independent data sets of earthquake focal mechanisms, volcanism, and, to an extent, the GPS vectors with the radial anisotropy model show reliability in our results and inferences. We now have a map of the areas undergoing extension and compression where we do not have direct measurements, such as beneath the sea; for example, the area undergoing extension beneath the Sicily Channel between MALT, LAMP, and Pantelleria (Figure 14).

### 4.4. Upper Mantle Dynamics: Thin Lithosphere and Vertical Mantle Flow

Direct evidence for deformation on a lithospheric-upper mantle scale is generally limited to seismic observations, often aided by models derived from analog and numerical methods. Beneath some areas such as Calabria, Sicily, and North Africa, radial anisotropy remains positive down to the maximum depth of our model (80 km), indicating that lateral deformation is vertically coherent throughout this depth range (Figure 11). Beneath the Tyrrhenian Sea and the Sicily Channel, there is a polarity change from positive radial anisotropy in the upper 10 km to negative anisotropy below 20 km, suggesting different patterns of deformation.

While the shallow deformation correlates with surface observations as discussed in the previous sections, the deeper negative anisotropy is more speculative. If mantle anisotropy is associated with the LPO of olivine and it is assumed to align parallel to the direction of mantle flow (Zhang & Karato, 1995), then the negative anisotropy indicates strain that is oriented vertical or subvertical. Olivine fabric transitions due to changes in water content, stress, and temperature (Karato et al., 2008) may also complicate the interpretation. A vertical mantle strain could develop from different scenarios: from a "passive" upward mantle flow replacing the new space created by the crustal/lithospheric thinning from far-field extensional stresses (e.g., Civile et al., 2010; Huismans et al., 2001), or from an "active" vertical flow of rising mantle that erodes the overlaying lithosphere (Huismans et al., 2001; Merle, 2011; Miller & Piana Agostinetti, 2011). Alternatively, a downward flow can also cause vertical mantle strain, especially underneath a slab tip from poloidal circulation (e.g., Funiciello et al., 2006).

Beneath the Tyrrhenian Sea, active mantle upwelling may have developed during the formation of volcanic fronts in the subduction zone (Davies & Stevenson, 1992; Tatsumi, 1986; Yogodzinski et al., 2001), or induced from a return flow and slab fragmentation associated with complex slab subduction (Faccenna et al., 2010) possibly involving rollback and break off gaps that result in toroidal and poloidal mantle circulation (e.g., Civello & Margheriti, 2004; Faccenna et al., 2007; Funiciello et al., 2003; Funiciello et al., 2006; Gvirtzman & Nur, 1999; Király et al., 2017, 2020; Merle, 2011; Piromallo et al., 2006; Trua et al., 2003), or from the dehydration of a stagnant slab below (Merle, 2011; Piromallo & Morelli, 2003). Thus, our observation of negative radial anisotropy and low shear velocities supports the hypothesis of mantle upwelling beneath the western Tyrrhenian Sea at least from 60 km depth (Figure 11) or shallower (Figure 13). Radial anisotropy at depths >60 km is unlikely to be well resolved in our model (Figure 11) because the Love-wave data have shorter periods than the Rayleigh waves, and thus the sensitivity of the radial anisotropy is limited to shallower depths (Figure S6 in Supporting Information S1). The change from positive to negative radial anisotropy may represent the LAB (Plomerová et al., 2002), which marks the base of the layer experiencing lateral extension above.

In the case of the Sicily Channel, the tectonic environment is different from the Tyrrhenian one because it is not located along the subduction zone and has no underlying stagnant slab. Instead, it is thought that the nearby subducted lithosphere has a slab window (or gap) which could affect the mantle circulation (e.g., Booth-Rea et al., 2018; Faccenna et al., 2007; Faccenna et al., 2011). We consider the recent surface-wave tomographic study of El-Sharkawy et al. (2020) (Figure 16), which shows strong low shear-velocity anomalies beneath the SCRZ, from 75 to 300 km depth (El-Sharkawy et al., 2021). Thus, the low velocity we observe beneath the SCRZ is

Figure 14. Crustal dynamics from volcanism, GPS vectors, earthquakes, and radial anisotropy. Background shade is the radial anisotropy at 5 km depth. (a) Comparison of radial anisotropy with intraplate (red) and subduction-related volcanism (blue) (Faccenna et al., 2005). (b) Horizontal GPS velocity vectors with respect to Eurasia (dark green arrows) (Bahrouni et al., 2020; Devoti et al., 2011). Vector differences between GPS stations across the Sicily Channel are shown in red arrows plotted midpoint between the station pairs, color-coded to match the respective reference stations LAMP (brown) and MALT (green). Note the difference in scales. (c) Extension (red sticks) and compression (blue sticks) components of the principal axes from the earthquake focal mechanism within the upper 10 km of the crust (European-Mediterranean Regional Centroid-Moment Tensors (Pondrelli, 2002)). The color of the focal mechanisms are as in Figure 11. Blue/red contours show the bathymetry/topography (ETOPO1, Amante & Eakins, 2009) at 250 m intervals with a median filter type of 100 km diameter (Wessel et al., 2019).
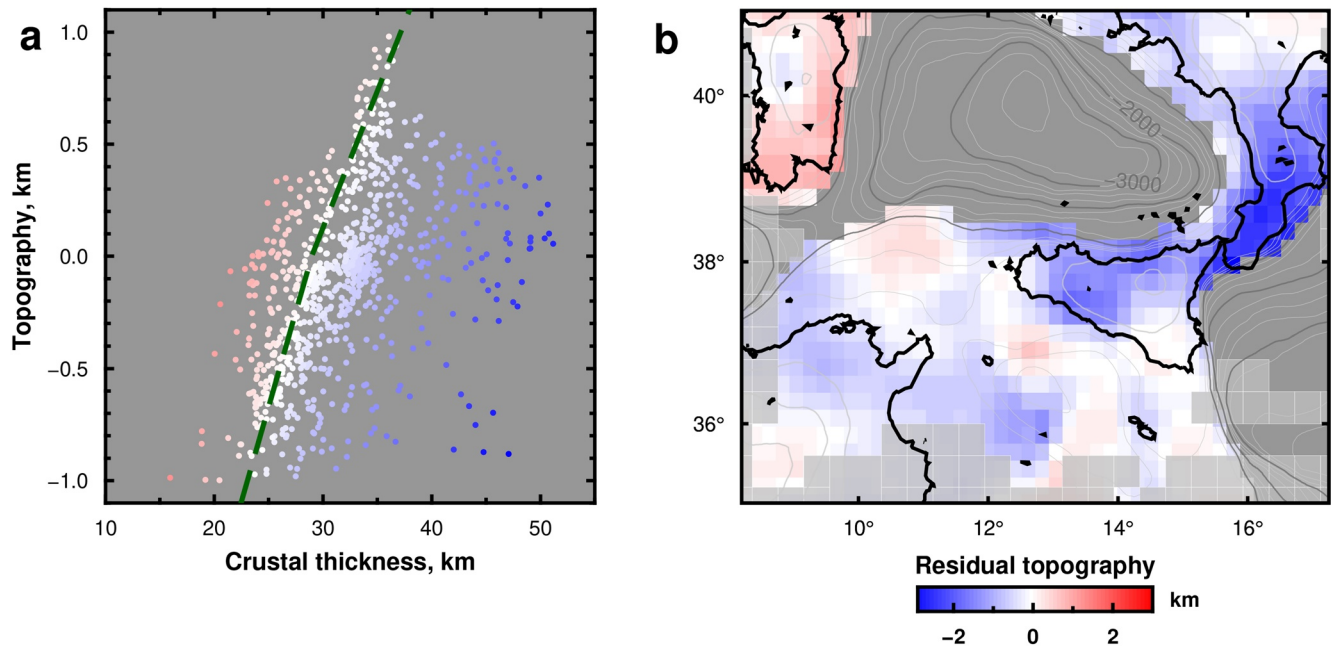
Figure 15. Crustal thickness, topography, and residual topography. (a) Crustal thickness versus topography. Each dot corresponds to a point on the crustal thickness map (Figure 10) for elevations greater than −1 km. Dashed green line is the crustal thickness versus topography relationship from Gvirtzman et al. (2016) inferred from a topography-crustal buoyancy prediction with a −1.1 km shift corresponding to the negative buoyancy of a 100 km-thick mantle lithosphere. Each dot is color-coded to indicate the difference of the smoothed ETOPO1 topography to the predicted topography for the different crustal thicknesses (e.g., Faccenna & Becker, 2020; Gvirtzman et al., 2016). (b) The difference between the ETOPO1 and predicted topography in (a) shown on a map. Red shade shows uplifted topography due to a thinner mantle lithosphere (Gvirtzman et al., 2016).

unlikely a result of passive vertical flow due to the rifting process above because, if so, the low V$_S$ would only be present a few tens of kilometers beneath the thinned lithosphere (e.g., West et al., 2004).

The low shear velocity in El-Sharkawy et al. (2020) is circumventing from southern to northern Sicily. The direction of mantle flow inferred from seismic shear-wave splitting (SKS) suggests a clockwise rotation from the front to the back of the Calabrian arc (Baccheschi et al., 2007, 2008; Civello & Margheriti, 2004; Faccenna et al., 2005, 2011; Lucente et al., 2006; Margheriti et al., 2003). The fast directions are described as toroidal mantle flow induced by rollback subduction (Civello & Margheriti, 2004). The anisotropic pattern is also confirmed from the uppermost mantle velocities of P_n (Mele et al., 1998) and S_n (Díaz et al., 2012), which suggest that the toroidal flow beneath the Sicily Channel is shallow starting from sub-Moho depths (Díaz et al., 2012). However, the depth range of the flow remains unclear (Zhu et al., 2015) as well as its orientation, whether it is purely horizontal, sub-horizontal, or subvertical (e.g., Faccenna et al., 2011). Our negative radial anisotropy in the upper mantle suggests that the toroidal flow has a vertical component and is concentrated within the SCRZ (Figures 11 and 13). Mantle upwelling beneath the Sicily Channel and adjacent areas may be related to poloidal flow from a retrograde slab motion as shown by numeric (e.g., Piromallo et al., 2006) and analog (e.g., Funiciello et al., 2006) models. The upwelling takes place at the slab edges as mantle material beneath the slab is displaced flowing laterally around the slab edges. This mechanism may also explain why the onset and peak of the negative anisotropy beneath the SCRZ are deeper than that of the western Tyrrhenian Sea (Figure 13).

The interplay between poloidal and toroidal fluxes is expected to produce uplift of the overriding plate and induce volcanism as a result of decompression melting (Faccenna et al., 2011). We look at the regional isostasy, the relationship of crustal thickness with topography, and compare with the prediction of crustal buoyancy for continents by Gvirtzman et al. (2016) (Figure 15). The prediction shows that the very thick crust beneath Calabria has a lower than expected topography in agreement with regional, large-scale dynamic topography models (e.g., Faccenna & Becker, 2020; Faccenna et al., 2014). In contrast, the thin crust of Sardinia has a higher than expected topography. The uplift of Sardinia has been previously determined from volcanic activity (Mariani et al., 2009), marine dating (Casini et al., 2020), and geomorphological studies (Demurtas et al., 2021). Parts of the SCRZ too show it is uplifted by a few hundreds of meters. The largest positive residual is located close to Pantelleria,
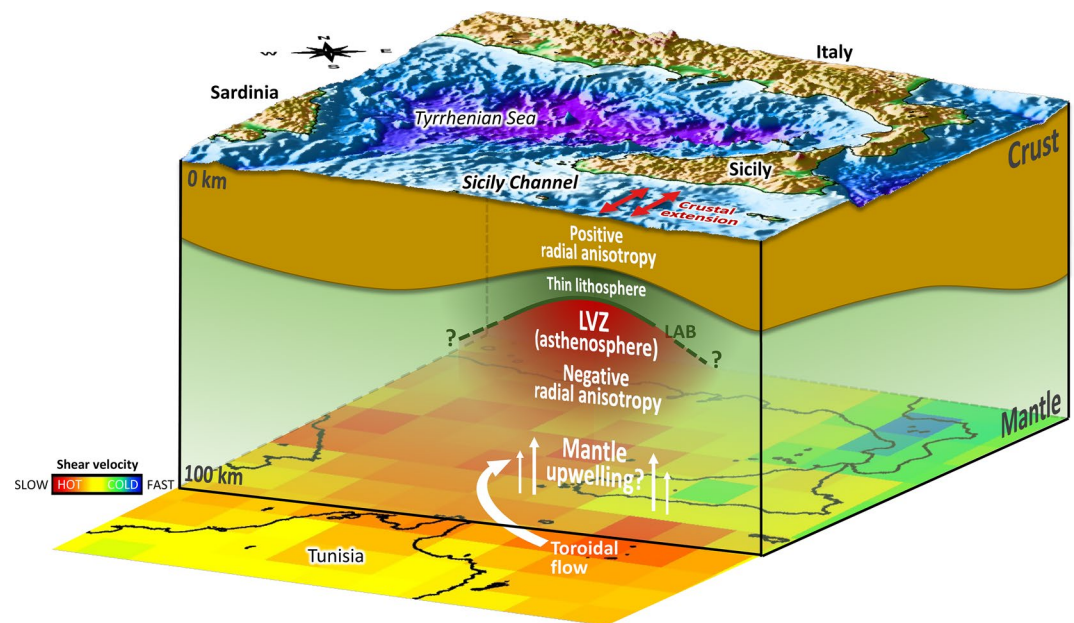
Figure 16. Summary of results. Vertical cross section along the Sicily Channel Rift Zone. Red arrows represent crustal extension inferred from differential GPS vectors at the surface, earthquake focal mechanisms, and from positive crustal radial anisotropy (Figures 14b and 14c). The crust and lithosphere beneath the SCRZ are thin, as inferred from the 1-D profiles, and are underlain by a low-velocity zone. The low-velocity zone (LVZ) is a proxy for a hot asthenosphere that facilitates vertical flow (white arrows), as suggested by the negative radial anisotropy. Bottom horizontal cross-section shows the shear velocity at 100 km depth from El-Sharkawy et al. (2020). Curved arrow shows the direction of mantle flow as inferred from SKS splitting (Civello & Margheriti, 2004).

an area that has active volcanism (Cavallaro & Coltelli, 2019; Lodolo et al., 2012; Parello et al., 2000), high heat flow (Vedova et al., 1995), and positive Bouguer (gravity) anomalies (Morelli et al., 1975). The uplift is likely a result of dynamic topography from the deflection of the surface due to active mantle flow (Faccenna & Becker, 2020). Evidence for mantle upwelling is corroborated with measured high concentration of Helium isotope ratios and high-heat flow originating from deep in the mantle (Caracausi et al., 2005; Civetta et al., 1998; Parello et al., 2000).

The new constraints from shear velocity and radial anisotropy confirm a more active mantle upwelling process than previously thought beneath the Sicily Channel. The upwelling is likely eroding, thinning, and stretching the lithosphere beneath the Channel. However, it remains unclear whether the upwelling is the only mechanism driving the rifting process or whether active upwelling is taking place simultaneously with shallow regional extensional forces (Magni et al., 2014). Furthermore, the faith of the SCRZ on how far the rift will extend in the future and if Sicily will become a separate tectonic microplate from Africa (Cello, 1987; Jongsma et al., 1985) remains to be seen.

5. Conclusions

We present a new isotropic 3-D shear-velocity and radial anisotropic model of the central Mediterranean, based on manually selected dispersion curves of fundamental mode Rayleigh and Love surface waves. The data is from ambient seismic noise recorded on several networks that operated for many years. Our results provide new constraints on the mantle dynamics in the region, particularly that of the Sicily Channel.

The shallow V_S structures coincide with topographic and tectonic features of the region: slow under high elevation mountain chains, fast beneath the deep sea. Inferred crustal thicknesses show general correlations with the elevation: thinnest beneath the deep basin of the Tyrrhenian Sea (~10 km) and thickest beneath the Apennine-Maghrebian mountain ranges (~50 km). The crust beneath Sardinia is 25–35 km thick, and thicker beneath Tunisia (35–40 km). Sicily is contrasted by a thick crust beneath the west-northwest mountain region and

a continental-type crust beneath the southeast (Hyblean Plateau). Across the Sicily Channel, the crustal thickness varies in the range of 18–25 km; the thinnest is beneath the SCRZ.

The shallow crustal radial anisotropy patterns have a good general agreement with the earthquake focal mechanisms, volcanic and tectonic features as well as GPS velocities. Areas experiencing compression (thrust) have negative anisotropy and subduction-related volcanism; areas experiencing extension have positive anisotropy and intraplate-related volcanism (Western Sardinia, the Tyrrhenian Sea, and the Sicily Channel). Positive seismic radial anisotropy highlights the extent of rifting across the Sicily Channel. The crustal radial anisotropy beneath the Channel is strong (+10%) and is located in an area actively undergoing SW–NE extension perpendicular to the normal faults and parallel to the extension component of earthquakes.

The lithosphere beneath the SCRZ is thin, underlain by low seismic shear velocities and negative radial anisotropy. The LAB rises from 60 km depth beneath Tunisia to ∼33 km beneath the SCRZ (Figure 13). We do not observe a LVZ or a mantle lid beneath the Tyrrhenian Sea, but a very low sub-Moho isotropic velocities that increase monotonically with depth. These zones of low shear velocities are a proxy for high temperatures that facilitate vertical flow, as inferred from the strong negative radial anisotropy (Figure 16). A deeper low shear velocity beneath the SCRZ (El-Sharkawy et al., 2020, 2021) suggests that upwelling has a mantle origin, possibly from poloidal flow that contributes to the negative radial anisotropy, volcanism, and an elevated residual topography.

While these results confirm an active upwelling and rifting process, it remains unclear whether the upwelling is the sole/dominant mechanism that is eroding, thinning, and stretching the lithosphere across the Sicily Channel or whether active upwelling is taking place simultaneously with shallow regional extensional forces.

Data Availability Statement

The raw seismic waveforms are available from the network repositories: IV (INGV Seismological Data Centre, 1997) (https://webservices.ingv.it/fdsnws/dataselect/1/), MN (MedNet Project Partner Institutions, 1988) (https://webservices.ingv.it/fdsnws/dataselect/1/), TT (Institut National de la Météorologie, 2008) (https://geofon.gfz-potsdam.de/fdsnws/dataselect/1/), YF (Suzan van der Lee et al., 1999 (http://service.iris.edu/irisws/fedcatalog/1/), and GE (GEOFON Data Centre, 1993) (https://geofon.gfz-potsdam.de/fdsnws/dataselect/1/. The software Obspy (Beyreuther et al., 2010), Geopsy (Wathelet et al., 2020), and SeisLib (Magrini et al., 2022) were used for the data processing. All figures were made using the Generic Mapping Tools (GMT) software (Agius, 2018; Wessel et al., 2019).

References

Agius, M. R. (2018). Getting started with GMT: An introduction for seismologists. In S. D'Amico (Ed.), *Moment tensor solutions: A useful tool for seismotectonics* (pp. 691–723). Springer International Publishing. https://doi.org/10.1007/978-3-319-77359-9_31

Agius, M. R., Galea, P., Farrugia, D., & D'Amico, S. (2020). An instrumental earthquake catalogue for the offshore Maltese islands region, 1995–2014. *Annals of Geophysics*, *63*(6), 658. https://doi.org/10.4401/ag-8383

Agius, M. R., & Lebedev, S. (2013). Tibetan and Indian lithospheres in the upper mantle beneath Tibet: Evidence from broadband surface-wave dispersion. *Geochemistry, Geophysics, Geosystems*, *14*(10), 4260–4281. https://doi.org/10.1002/ggge.20274

Agius, M. R., & Lebedev, S. (2014). Shear-velocity structure, radial anisotropy and dynamics of the Tibetan crust. *Geophysical Journal International*, *199*(3), 1395–1415. https://doi.org/10.1093/gji/ggu326

Agius, M. R., & Lebedev, S. (2017). Complex, multilayered azimuthal anisotropy beneath Tibet: Evidence for co-existing channel flow and pure-shear crustal thickening. *Geophysical Journal International*, *210*(3), 1823–1844. https://doi.org/10.1093/gji/ggx266

Aki, K. (1957). Space and time spectra of stationary stochastic waves, with special reference to microtremors. *Bulletin of Earthquake Research Institute*, *35*, 415–456.

Aki, K., & Richards, P. G. (2002). *Quantitative seismology*. University Science Books.

Alder, C., Debayle, E., Bodin, T., Paul, A., Stehly, L., Pedersen, H., & The AlpArray Working Group (2021). Evidence for radial anisotropy in the lower crust of the Apennines from Bayesian ambient noise tomography in Europe. *Geophysical Journal International*, *226*(2), 941–967. https://doi.org/10.1093/gji/ggab066

Alessandrini, B., Beranzoli, L., & Mele, F. M. (1995). 3-D crustal P-wave velocity tomography of the Italian region using local and regional seismicity data. *Annals of Geophysics*, *38*(2). https://doi.org/10.4401/ag-4119

Amante, C., & Eakins, B. W. (2009). Etopo1 arc-minute global relief model: Procedures, data sources and analysis.

Anzidei, M., Baldi, P., Casula, G., Galvani, A., Mantovani, E., Pesci, A., et al. (2001). Insights into present-day crustal motion in the central Mediterranean area from GPS surveys. *Geophysical Journal International*, *146*(1), 98–110. https://doi.org/10.1046/j.0956-540x.2001.01425.x

Argnani, A. (1990). The strait of Sicily rift zone: Foreland deformation related to the evolution of a back-arc basin. *Journal of Geodynamics*, *12*(2), 311–331. https://doi.org/10.1016/0264-3707(90)90028-S

Baccheschi, P., Margheriti, L., & Steckler, M. (2008). SKS splitting in southern Italy: Anisotropy variations in a fragmented subduction zone. *Tectonophysics*, *462*(1), 49–67. https://doi.org/10.1016/j.tecto.2007.10.014

Baccheschi, P., Margheriti, L., & Steckler, M. S. (2007). Seismic anisotropy reveals focused mantle flow around the Calabrian slab (southern Italy). *Geophysical Research Letters*, *34*(5). https://doi.org/10.1029/2006GL028899

Bahrouni, N., Masson, F., Meghraoui, M., Saleh, M., Maamri, R., Dhaha, F., & Arfaoui, M. (2020). Active tectonics and GPS data analysis of the Maghrebian thrust belt and Africa-Eurasia plate convergence in Tunisia. *Tectonophysics*, *785*, 228440. https://doi.org/10.1016/j.tecto.2020.228440

Barberi, G., Cosentino, M., Gervasi, A., Guerra, I., Neri, G., & Orecchio, B. (2004). Crustal seismic tomography in the Calabrian arc region, south Italy. *Physics of the Earth and Planetary Interiors*, *147*(4), 297–314. https://doi.org/10.1016/j.pepi.2004.04.005

Bensen, G. D., Ritzwoller, M. H., Barmin, M. P., Levshin, A. L., Lin, F., Moschetti, M. P., et al. (2007). Processing seismic ambient noise data to obtain reliable broad-band surface wave dispersion measurements. *Geophysical Journal International*, *169*(3), 1239–1260. https://doi.org/10.1111/j.1365-246X.2007.03374.x

Beyreuther, M., Barsch, R., Krischer, L., Megies, T., Behr, Y., & Wassermann, J. (2010). ObsPy: A Python toolbox for seismology. *Seismological Research Letters*, *81*(3), 530–533. https://doi.org/10.1785/gssrl.81.3.530

Blom, N., Gokhberg, A., & Fichtner, A. (2020). Seismic waveform tomography of the central and eastern Mediterranean upper mantle. *Solid Earth*, *11*(2), 669–690. https://doi.org/10.5194/se-11-669-2020

Boccaletti, M., Cello, G., & Tortorici, L. (1987). Transtensional tectonics in the Sicily channel. *Journal of Structural Geology*, *9*(7), 869–876. https://doi.org/10.1016/0191-8141(87)90087-3

Bodin, T., Sambridge, M., Rawlinson, N., & Arroucau, P. (2012). Transdimensional tomography with unknown data noise. *Geophysical Journal International*, *189*(3), 1536–1556. https://doi.org/10.1111/j.1365-246X.2012.05414.x

Bondár, I., Myers, S. C., Engdahl, E. R., & Bergman, E. A. (2004). Epicentre accuracy based on seismic network criteria. *Geophysical Journal International*, *156*(3), 483–496. https://doi.org/10.1111/j.1365-246X.2004.02070.x

Booth-Rea, G., Gaidi, S., Melki, F., Marzougui, W., Azañón, J. M., Zargouni, F., et al. (2018). Late miocene extensional collapse of northern Tunisia. *Tectonics*, *37*(6), 1626–1647. https://doi.org/10.1029/2017TC004846

Boschi, L., & Dziewonski, A. M. (1999). High- and low-resolution images of the Earth's mantle: Implications of different approaches to tomographic modeling. *Journal of Geophysical Research*, *104*(B11), 25567–25594. https://doi.org/10.1029/1999JB900166

Boschi, L., Fry, B., Ekström, G., & Giardini, D. (2009). The European upper mantle as seen by surface waves. *Surveys in Geophysics*, *30*(4), 463–501. https://doi.org/10.1007/s10712-009-9066-2

Calò, M., & Parisi, L. (2014). Evidences of a lithospheric fault zone in the Sicily Channel continental rift (southern Italy) from instrumental seismicity data. *Geophysical Journal International*, *199*(1), 219–225. https://doi.org/10.1093/gji/ggu249

Calò, M., Parisi, L., & Luzio, D. (2013). Lithospheric P- and S-wave velocity models of the Sicilian area using WAM tomography: Procedure and assessments. *Geophysical Journal International*, *195*(1), 625–649. https://doi.org/10.1093/gji/ggt252

Caracausi, A., Favara, R., Italiano, F., Nuccio, P. M., Paonita, A., & Rizzo, A. (2005). Active geodynamics of the central Mediterranean sea: Tensional tectonic evidences in Western Sicily from mantle-derived helium. *Geophysical Research Letters*, *32*(4). https://doi.org/10.1029/2004GL021608

Carminati, E., Lustrino, M., & Doglioni, C. (2012). Geodynamic evolution of the central and Western Mediterranean: Tectonics vs. igneous petrology constraints. *Tectonophysics*, *579*, 173–192. https://doi.org/10.1016/j.tecto.2012.01.026

Carminati, E., Wortel, M., Meijer, P., & Sabadini, R. (1998). The two-stage opening of the western–central Mediterranean basins: A forward modeling test to a new evolutionary model. *Earth and Planetary Science Letters*, *160*(3), 667–679. https://doi.org/10.1016/S0012-821X(98)00119-8

Carminati, E., Wortel, M., Spakman, W., & Sabadini, R. (1998). The role of slab detachment processes in the opening of the western–central Mediterranean basins: Some geological and geophysical evidence. *Earth and Planetary Science Letters*, *160*(3), 651–665. https://doi.org/10.1016/S0012-821X(98)00118-6

Casini, L., Andreucci, S., Sechi, D., Huang, C.-Y., Shen, C.-C., & Pascucci, V. (2020). Luminescence dating of late Pleistocene faults as evidence of uplift and active tectonics in Sardinia, W Mediterranean. *Terra Nova*, *32*(4), 261–271. https://doi.org/10.1111/ter.12458

Catalano, R., Di Stefano, P., Sulli, A., & Vitale, F. (1996). Paleogeography and structure of the central Mediterranean: Sicily and its offshore area. *Tectonophysics*, *260*(4), 291–323. https://doi.org/10.1016/0040-1951(95)00196-4

Cavallaro, D., & Coltelli, M. (2019). The graham volcanic field offshore southwestern Sicily (Italy) revealed by high-resolution seafloor mapping and rov images. *Frontiers of Earth Science*, *7*, 311. https://doi.org/10.3389/feart.2019.00311

Cella, F., Fedi, M., Florio, G., & Rapolla, A. (1998). Gravity modelling of the litho-asthenosphere system in the Central Mediterranean. *Tectonophysics*, *287*(1), 117–138. https://doi.org/10.1016/S0040-1951(98)80064-4

Cello, G. (1987). Structure and deformation processes in the Strait of Sicily "rift zone". *Tectonophysics*, *141*(1), 237–247. https://doi.org/10.1016/0040-1951(87)90188-0

Chiarabba, C., Jovane, L., & DiStefano, R. (2005). A new view of Italian seismicity using 20 years of instrumental recordings. *Tectonophysics*, *395*(3), 251–268. https://doi.org/10.1016/j.tecto.2004.09.013

Cimini, G. B. (1999). P-wave deep velocity structure of the southern Tyrrhenian subduction zone from nonlinear teleseismic traveltime tomography. *Geophysical Research Letters*, *26*(24), 3709–3712. https://doi.org/10.1029/1999GL010907

Cimini, G. B., & Gori, P. D. (1997). Upper mantle velocity structure beneath Italy from direct and secondary P-wave teleseismic tomography. *Annals of Geophysics*, *40*(1). https://doi.org/10.4401/ag-3944

Cimini, G. B., & Marchetti, A. (2006). Deep structure of peninsular Italy from seismic tomography and subcrustal seismicity.

Civello, S., & Margheriti, L. (2004). Toroidal mantle flow around the Calabrian slab (Italy) from SKS splitting. *Geophysical Research Letters*, *31*(10). https://doi.org/10.1029/2004GL019607

Civetta, L., D'Antonio, M., Orsi, G., & Tilton, G. R. (1998). The geochemistry of volcanic rocks from Pantelleria Island, Sicily Channel: Petrogenesis and characteristics of the mantle source region. *Journal of Petrology*, *39*(8), 1453–1491. https://doi.org/10.1093/petroj/39.8.1453

Civile, D., Lodolo, E., Accaino, F., Geletti, R., Schiattarella, M., Giustiniani, M., et al. (2018). Capo Granitola-Sciacca Fault Zone (Sicilian Channel, Central Mediterranean): Structure vs magmatism. *Marine and Petroleum Geology*, *96*, 627–644. https://doi.org/10.1016/j.marpetgeo.2018.05.016

Civile, D., Lodolo, E., Accettella, D., Geletti, R., Ben-Avraham, Z., Deponte, M., et al. (2010). The Pantelleria graben (Sicily Channel, Central Mediterranean): An example of intraplate 'passive' rift. *Tectonophysics*, *490*(3), 173–183. https://doi.org/10.1016/j.tecto.2010.05.008

Civile, D., Lodolo, E., Tortorici, L., Lanzafame, G., & Brancolini, G. (2008). Relationships between magmatism and tectonics in a continental rift: The Pantelleria Island region (Sicily Channel, Italy). *Marine Geology*, *251*(1), 32–46. https://doi.org/10.1016/j.margeo.2008.01.009

Corti, G., Cuffaro, M., Doglioni, C., Innocenti, F., & Manetti, P. (2006). Coexisting geodynamic processes in the Sicily Channel. In *Postcollisional tectonics and magmatism in the Mediterranean region and Asia*. Geological Society of America. https://doi.org/10.1130/2006.2409(05)

Crampin, S., & Chastin, S. (2003). A review of shear wave splitting in the crack-critical crust. *Geophysical Journal International*, *155*(1), 221–240. https://doi.org/10.1046/j.1365-246X.2003.02037.x

D'Agostino, N., & Selvaggi, G. (2004). Crustal motion along the Eurasia-Nubia plate boundary in the Calabrian Arc and Sicily and active extension in the Messina Straits from GPS measurements. *Journal of Geophysical Research*, *109*(B11). https://doi.org/10.1029/2004JB002998

D'Alessandro, A., Luzio, D., D'Anna, G., & Mangano, G. (2011). Seismic network evaluation through simulation: An application to the Italian national seismic network. *Bulletin of the Seismological Society of America*, *101*(3), 1213–1232. https://doi.org/10.1785/0120100066

Davies, J. H., & Stevenson, D. J. (1992). Physical model of source region of subduction zone volcanics. *Journal of Geophysical Research*, *97*(B2), 2037–2070. https://doi.org/10.1029/91JB02571

Demurtas, V., Orrù, P. E., & Deiana, G. (2021). Evolution of deep-seated gravitational slope deformations in relation with uplift and fluvial capture processes in central eastern sardinia (Italy). *Land*, *10*(11), 1193. https://doi.org/10.3390/land10111193

Devoti, R., Esposito, A., Pietrantonio, G., Pisani, A. R., & Riguzzi, F. (2011). Evidence of large scale deformation patterns from GPS data in the Italian subduction boundary. *Earth and Planetary Science Letters*, *311*(3), 230–241. https://doi.org/10.1016/j.epsl.2011.09.034

Dewey, J. F., Helman, M. L., Knott, S. D., Turco, E., & Hutton, D. H. W. (1989). Kinematics of the Western Mediterranean. *Geological Society, London*, *45*(1), 265–283. https://doi.org/10.1144/GSL.SP.1989.045.01.15

Díaz, J., Gil, A., & Gallart, J. (2012). Uppermost mantle seismic velocity and anisotropy in the Euro-Mediterranean region from Pn and Sn tomography. *Geophysical Journal International*, *192*(1), 310–325. https://doi.org/10.1093/gji/ggs016

Di Stefano, R., Bianchi, I., Ciaccio, M. G., Carrara, G., & Kissling, E. (2011). Three-dimensional Moho topography in Italy: New constraints from receiver functions and controlled source seismology. *Geochemistry, Geophysics, Geosystems*, *12*(9). https://doi.org/10.1029/2011GC003649

Dziewoński, A., Chou, T.-A., & Woodhouse, J. (1981). Determination of earthquake source parameters from waveform data for studies of global and regional seismicity. *Journal of Geophysical Research*, *86*(B4), 2825–2852. https://doi.org/10.1029/jb086ib04p02825

Eaton, D. W., Darbyshire, F., Evans, R. L., Grütter, H., Jones, A. G., & Yuan, X. (2009). The elusive lithosphere–asthenosphere boundary (lab) beneath cratons. *Lithos*, *109*(1), 1–22. https://doi.org/10.1016/j.lithos.2008.05.009

Ekström, G., Abers, G. A., & Webb, S. C. (2009). Determination of surface-wave phase velocities across usarray from noise and aki's spectral formulation. *Geophysical Research Letters*, *36*(18), L18301. https://doi.org/10.1029/2009GL039131

El-Sharkawy, A., Meier, T., Hübscher, C., Lebedev, S., Dannowski, A., Kopp, H., et al. (2021). Lithospheric structure of the eastern Mediterranean Sea: Inferences from surface wave tomography and stochastic inversions constrained by wide-angle refraction measurements. *Tectonophysics*, *821*, 229159. https://doi.org/10.1016/j.tecto.2021.229159

El-Sharkawy, A., Meier, T., Lebedev, S., Behrmann, J. H., Hamada, M., Cristiano, L., et al. (2020). The slab puzzle of the alpine-Mediterranean region: Insights from a new, high-resolution, shear wave velocity model of the upper mantle. *Geochemistry, Geophysics, Geosystems*, *21*(8), e2020GC008993. https://doi.org/10.1029/2020GC008993

Faccenda, M., Gerya, T. V., Mancktelow, N. S., & Moresi, L. (2012). Fluid flow during slab unbending and dehydration: Implications for intermediate-depth seismicity, slab weakening and deep water recycling. *Geochemistry, Geophysics, Geosystems*, *13*(1). https://doi.org/10.1029/2011GC003860

Faccenna, C., & Becker, T. W. (2020). Topographic expressions of mantle dynamics in the Mediterranean. *Earth-Science Reviews*, *209*, 103327. https://doi.org/10.1016/j.earscirev.2020.103327

Faccenna, C., Becker, T. W., Auer, L., Billi, A., Boschi, L., Brun, J. P., et al. (2014). Mantle dynamics in the Mediterranean. *Reviews of Geophysics*, *52*(3), 283–332. https://doi.org/10.1002/2013RG000444

Faccenna, C., Becker, T. W., Lallemand, S., Lagabrielle, Y., Funiciello, F., & Piromallo, C. (2010). Subduction-triggered magmatic pulses: A new class of plumes? *Earth and Planetary Science Letters*, *299*(1), 54–68. https://doi.org/10.1016/j.epsl.2010.08.012

Faccenna, C., Becker, T. W., Miller, M. S., Serpelloni, E., & Willett, S. D. (2014). Isostasy, dynamic topography, and the elevation of the apennines of Italy. *Earth and Planetary Science Letters*, *407*, 163–174. https://doi.org/10.1016/j.epsl.2014.09.027

Faccenna, C., Civetta, L., D'Antonio, M., Funiciello, F., Margheriti, L., & Piromallo, C. (2005). Constraints on mantle circulation around the deforming Calabrian slab. *Geophysical Research Letters*, *32*(6), L06311. https://doi.org/10.1029/2004GL021874

Faccenna, C., Funiciello, F., Civetta, L., D'Antonio, M., Moroni, M., & Piromallo, C. (2007). Slab disruption, mantle circulation, and the opening of the Tyrrhenian basins. In *Cenozoic volcanism in the Mediterranean area*. Geological Society of America. https://doi.org/10.1130/2007.2418(08)

Faccenna, C., Funiciello, F., Giardini, D., & Lucente, P. (2001). Episodic back-arc extension during restricted mantle convection in the central Mediterranean. *Earth and Planetary Science Letters*, *187*(1), 105–116. https://doi.org/10.1016/S0012-821X(01)00280-1

Faccenna, C., Molin, P., Orecchio, B., Olivetti, V., Bellier, O., Funiciello, F., et al. (2011). Topography of the Calabria subduction zone (southern Italy): Clues for the origin of Mt. Etna. *Tectonics*, *30*(1), 2010TC002694. https://doi.org/10.1029/2010TC002694

Finetti, I. (1985). Structure and evolution of the central Mediterranean (Pelagian and Ionian seas). In *Geological evolution of the Mediterranean basin* (pp. 215–230). Springer. https://doi.org/10.1007/978-1-4613-8572-1_10

Frohlich, C. (1992). Triangle diagrams: Ternary graphs to display similarity and diversity of earthquake focal mechanisms. *Physics of the Earth and Planetary Interiors*, *75*(1), 193–198. https://doi.org/10.1016/0031-9201(92)90130-N

Fullea, J., Lebedev, S., Agius, M. R., Jones, A. G., & Afonso, J. C. (2012). Lithospheric structure in the Baikal–central Mongolia region from integrated geophysical-petrological inversion of surface-wave data and topographic elevation. *Geochemistry, Geophysics, Geosystems*, *13*(8). https://doi.org/10.1029/2012GC004138

Funiciello, F., Faccenna, C., Giardini, D., & Regenauer-Lieb, K. (2003). Dynamics of retreating slabs: 2. Insights from three-dimensional laboratory experiments. *Journal of Geophysical Research*, *108*(B4). https://doi.org/10.1029/2001JB000896

Funiciello, F., Moroni, M., Piromallo, C., Faccenna, C., Cenedese, A., & Bui, H. A. (2006). Mapping mantle flow during retreating subduction: Laboratory models analyzed by feature tracking. *Journal of Geophysical Research*, *111*(B3). https://doi.org/10.1029/2005JB003792

GEOFON Data Centre. (1993). *Geofon seismic network*. Deutsches GeoForschungsZentrum GFZ. https://doi.org/10.14470/TR560404

Giacomuzzi, G., Civalleri, M., De Gori, P., & Chiarabba, C. (2012). A 3D Vs model of the upper mantle beneath Italy: Insight on the geodynamics of central Mediterranean. *Earth and Planetary Science Letters*, *335–336*, 105–120. https://doi.org/10.1016/j.epsl.2012.05.004

Goes, S., Giardini, D., Jenny, S., Hollenstein, C., Kahle, H.-G., & Geiger, A. (2004). A recent tectonic reorganization in the south-central Mediterranean. *Earth and Planetary Science Letters*, *226*(3), 335–345. https://doi.org/10.1016/j.epsl.2004.07.038

Grad, M., Tiira, T., & Group, E. W. (2009). The Moho depth map of the European Plate. *Geophysical Journal International*, *176*(1), 279–292. https://doi.org/10.1111/j.1365-246X.2008.03919.x

Greve, S., Paulssen, H., Goes, S., & van Bergen, M. (2014). Shear-velocity structure of the Tyrrhenian sea: Tectonics, volcanism and mantle (de)hydration of a back-arc basin. *Earth and Planetary Science Letters*, *400*, 45–53. https://doi.org/10.1016/j.epsl.2014.05.028

Gualtieri, L., Bachmann, E., Simons, F. J., & Tromp, J. (2021). Generation of secondary microseism Love waves: Effects of bathymetry, 3-D structure and source seasonality. *Geophysical Journal International*, *226*(1), 192–219. https://doi.org/10.1093/gji/ggab095

Gvirtzman, Z., Faccenna, C., & Becker, T. W. (2016). Isostasy, flexure, and dynamic topography. *Tectonophysics*, *683*, 255–271. https://doi.org/10.1016/j.tecto.2016.05.041

Gvirtzman, Z., & Nur, A. (1999). The formation of Mount Etna as the consequence of slab rollback. *Nature*, *401*(6755), 782–785. https://doi.org/10.1038/44555

Hansen, P. C. (2001). The L-curve and its use in the numerical treatment of inverse problems. In in *Computational inverse problems in electro-cardiology*, ed. In P. Johnston (Ed.),, *Advances in computational bioengineering* (pp. 119–142). WIT Press.

Huismans, R. S., Podladchikov, Y. Y., & Cloetingh, S. (2001). Transition from passive to active rifting: Relative importance of asthenospheric doming and passive extension of the lithosphere. *Journal of Geophysical Research*, *106*(B6), 11271–11291. https://doi.org/10.1029/2000JB900424

INGV Seismological Data Centre. (1997). *Rete sismica nazionale (RSN)*. Istituto Nazionale di Geofisica e Vulcanologia (INGV). https://doi.org/10.13127/SD/X0FXNH7QFY

Institut National de la Météorologie (2008). *Seismic network of Tunisia*. Institut National de la Météorologie. Retrieved from https://www.meteo.tn/

International Seismological Centre. (2021). On-line bulletin. https://doi.org/10.31905/D808B830

Jongsma, D., van Hinte, J. E., & Woodside, J. M. (1985). Geologic structure and neotectonics of the North African continental margin south of Sicily. *Marine and Petroleum Geology*, *2*(2), 156–179. https://doi.org/10.1016/0264-8172(85)90005-4

Karato, S. (2012). On the origin of the asthenosphere. *Earth and Planetary Science Letters*, *321–322*, 95–103. https://doi.org/10.1016/j.epsl.2012.01.001

Karato, S., & Jung, H. (1998). Water, partial melting and the origin of the seismic low velocity and high attenuation zone in the upper mantle. *Earth and Planetary Science Letters*, *157*(3), 193–207. https://doi.org/10.1016/S0012-821X(98)00034-X

Karato, S.-I., Jung, H., Katayama, I., & Skemer, P. (2008). Geodynamic significance of seismic anisotropy of the upper mantle: New insights from laboratory studies. *Annual Review of Earth and Planetary Sciences*, *36*(1), 59–95. https://doi.org/10.1146/annurev.earth.36.031207.124120

Kästle, E. D., El-Sharkawy, A., Boschi, L., Meier, T., Rosenberg, C., Bellahsen, N., et al. (2018). Surface wave tomography of the Alps using ambient-noise and earthquake phase velocity measurements. *Journal of Geophysical Research*, *123*(2), 1770–1792. https://doi.org/10.1002/2017JB014698

Kästle, E. D., Soomro, R., Weemstra, C., Boschi, L., & Meier, T. (2016). Two-receiver measurements of phase velocity: Cross-validation of ambient-noise and earthquake-based observations. *Geophysical Journal International*, *207*(3), 1493–1512. https://doi.org/10.1093/gji/ggw341

Kennett, B. L. N., & Engdahl, E. R. (1991). Traveltimes for global earthquake location and phase identification. *Geophysical Journal International*, *105*(2), 429–465. https://doi.org/10.1111/j.1365-246X.1991.tb06724.x

Kherchouche, R., Ouyed, M., Aoudia, A., Mellouk, B., & Saadi, A. (2020). Structure of the crust and uppermost mantle beneath the Sicily channel from ambient noise and earthquake tomography. *Annals of Geophysics*, *63*(6), 666. https://doi.org/10.4401/ag-8356

Khomsi, S., de Lamotte, D. F., Bédir, M., & Echihi, O. (2016). The late eocene and late miocene fronts of the atlas belt in eastern Maghreb: Integration in the geodynamic evolution of the Mediterranean domain. *Arabian Journal of Geosciences*, *9*(15), 650. https://doi.org/10.1007/s12517-016-2609-1

Kincaid, C., & Griffiths, R. W. (2003). Laboratory models of the thermal evolution of the mantle during rollback subduction. *Nature*, *425*(6953), 58–62. https://doi.org/10.1038/nature01923

Király, A., Capitanio, F. A., Funiciello, F., & Faccenna, C. (2017). Subduction induced mantle flow: Length-scales and orientation of the toroidal cell. *Earth and Planetary Science Letters*, *479*, 284–297. https://doi.org/10.1016/j.epsl.2017.09.017

Király, A., Portner, D. E., Haynie, K. L., Chilson-Parks, B. H., Ghosh, T., Jadamec, M., et al. (2020). The effect of slab gaps on subduction dynamics and mantle upwelling. *Tectonophysics*, *785*, 228458. https://doi.org/10.1016/j.tecto.2020.228458

Li, H., Bernardi, F., & Michelini, A. (2010). Surface wave dispersion measurements from ambient seismic noise analysis in Italy. *Geophysical Journal International*, *180*(3), 1242–1252. https://doi.org/10.1111/j.1365-246X.2009.04476.x

Lindenfeld, M., & Rümpker, G. (2011). Detection of mantle earthquakes beneath the East African Rift. *Geophysical Journal International*, *186*(1), 1–5. https://doi.org/10.1111/j.1365-246X.2011.05048.x

Lindenfeld, M., Rümpker, G., Batte, A., & Schumann, A. (2012). Seismicity from february 2006 to september 2007 at the rwenzori mountains, East African rift: Earthquake distribution, magnitudes and source mechanisms. *Solid Earth*, *3*(2), 251–264. https://doi.org/10.5194/se-3-251-2012

Lodolo, E., Civile, D., Zanolla, C., & Geletti, R. (2012). Magnetic signature of the Sicily Channel volcanism. *Marine Geophysical Researches*, *33*(1), 33–44. https://doi.org/10.1007/s11001-011-9144-y

Lu, Y., Stehly, L., Paul, A., & Group, A. W. (2018). High-resolution surface wave tomography of the European crust and uppermost mantle from ambient seismic noise. *Geophysical Journal International*, *214*(2), 1136–1150. https://doi.org/10.1093/gji/ggy188

Lucente, F. P., Chiarabba, C., Cimini, G. B., & Giardini, D. (1999). Tomographic constraints on the geodynamic evolution of the Italian region. *Journal of Geophysical Research*, *104*(B9), 20307–20327. https://doi.org/10.1029/1999JB900147

Lucente, F. P., Margheriti, L., Piromallo, C., & Barruol, G. (2006). Seismic anisotropy reveals the long route of the slab through the western-central Mediterranean mantle. *Earth and Planetary Science Letters*, *241*(3), 517–529. https://doi.org/10.1016/j.epsl.2005.10.041

Magni, V., Faccenna, C., van Hunen, J., & Funiciello, F. (2014). How collision triggers backarc extension: Insight into Mediterranean style of extension from 3-d numerical models. *Geology*, *42*(6), 511–514. https://doi.org/10.1130/g35446.1

Magrini, F., & Boschi, L. (2021). Surface-wave attenuation from seismic ambient noise: Numerical validation and application. *Journal of Geophysical Research*, *126*(1). https://doi.org/10.1029/2020JB019865

Magrini, F., Diaferia, G., Boschi, L., & Cammarano, F. (2019). Arrival-angle effects on two-receiver measurements of phase velocity. *Geophysical Journal International*, *220*(3), 1838–1844. https://doi.org/10.1093/gji/ggz560

Magrini, F., Diaferia, G., El-Sharkawy, A., Cammarano, F., van der Meijde, M., Meier, T., & Boschi, L. (2022). Surface-wave tomography of the central-western Mediterranean: New insights into the Liguro-Provençal and Tyrrhenian basins. *Journal of Geophysical Research*, *127*(3). https://doi.org/10.1029/2021JB023267

Magrini, F., Diaferia, G., Fadel, I., Cammarano, F., van der Meijde, M., & Boschi, L. (2019). 3-D shear wave velocity model of the lithosphere below the Sardinia–Corsica continental block based on Rayleigh-wave phase velocities. *Geophysical Journal International*, *220*(3), 2119–2130. https://doi.org/10.1093/gji/ggz555

Magrini, F., Lauro, S., Kästle, E., & Boschi, L. (2022). Surface-wave tomography using SeisLib: A Python package for multiscale seismic imaging. *Geophysical Journal International*, *231*(2), 1011–1030. https://doi.org/10.1093/gji/ggac236

Malinverno, A., & Ryan, W. B. F. (1986). Extension in the Tyrrhenian Sea and shortening in the apennines as result of arc migration driven by sinking of the lithosphere. *Tectonics*, *5*(2), 227–245. https://doi.org/10.1029/TC005i002p00227

Manu-Marfo, D., Aoudia, A., Pachhai, S., & Kherchouche, R. (2019). 3D shear wave velocity model of the crust and uppermost mantle beneath the Tyrrhenian basin and margins. *Scientific Reports*, *9*(1), 1–10. https://doi.org/10.1038/s41598-019-40510-z

Margheriti, L., Lucente, F. P., & Pondrelli, S. (2003). SKS splitting measurements in the Apenninic-Tyrrhenian domain (Italy) and their relation with lithospheric subduction and mantle convection. *Journal of Geophysical Research*, *108*(B4). https://doi.org/10.1029/2002JB001793

Mariani, P., Braitenberg, C., & Antonioli, F. (2009). Sardinia coastal uplift and volcanism. *Pure and Applied Geophysics*, *166*(8–9), 1369–1402. https://doi.org/10.1007/s00024-009-0504-3

Marone, F., van der Meijde, M., van der Lee, S., & Giardini, D. (2003). Joint inversion of local, regional and teleseismic data for crustal thickness in the Eurasia–Africa plate boundary region. *Geophysical Journal International*, *154*(2), 499–514. https://doi.org/10.1046/j.1365-246X.2003.01973.x

McClusky, S., Reilinger, R., Mahmoud, S., Ben Sari, D., & Tealeb, A. (2003). GPS constraints on Africa (Nubia) and Arabia plate motions. *Geophysical Journal International*, *155*(1), 126–138. https://doi.org/10.1046/j.1365-246X.2003.02023.x

MedNet Project Partner Institutions. (1988). Mediterranean very broadband seismographic network (MedNet). Istituto Nazionale di Geofisica e Vulcanologia (INGV). https://doi.org/10.13127/SD/FBBBTDTD6Q

Mele, G., Rovelli, A., Seber, D., Hearn, T., & Barazangi, M. (1998). Compressional velocity structure and anisotropy in the uppermost mantle beneath Italy and surrounding regions. *Journal of Geophysical Research*, *103*(B6), 12529–12543. https://doi.org/10.1029/98jb00596

Merle, O. (2011). A simple continental rift classification. *Tectonophysics*, *513*(1), 88–95. https://doi.org/10.1016/j.tecto.2011.10.004

Milano, M., Kelemework, Y., La Manna, M., Fedi, M., Montanari, D., & Iorio, M. (2020). Crustal structure of Sicily from modelling of gravity and magnetic anomalies. *Scientific Reports*, *10*(1), 1–18. https://doi.org/10.1038/s41598-020-72849-z

Miller, M. S., & Piana Agostinetti, N. (2011). Erosion of the continental lithosphere at the cusps of the Calabrian arc: Evidence from *S* receiver functions analysis. *Geophysical Research Letters*, *38*(23). https://doi.org/10.1029/2011GL049455

Molinari, I., & Morelli, A. (2011). EPcrust: A reference crustal model for the European plate. *Geophysical Journal International*, *185*(1), 352–364. https://doi.org/10.1111/j.1365-246x.2011.04940.x

Monna, S., Montuori, C., Piromallo, C., & Vinnik, L. (2019). Mantle structure in the central Mediterranean region from *P* and *S* receiver functions. *Geochemistry, Geophysics, Geosystems*, *20*(10), 4545–4566. https://doi.org/10.1029/2019GC008496

Montuori, C., Cimini, G. B., & Favali, P. (2007). Teleseismic tomography of the southern Tyrrhenian subduction zone: New results from seafloor and land recordings. *Journal of Geophysical Research*, *112*(B3), B03311. https://doi.org/10.1029/2005jb004114

Morelli, C., Gantar, C., & Pisani, M. (1975). Bathymetry, gravity and magnetism in the straits of Sicily and Ionian sea. *Bollettino di Geofisica Teorica ed Applicata*, *17*, 39–58.

Morelli, C., & Nicolich, R. (1990). A cross section of the lithosphere along the European geotraverse southern segment (from the Alps to Tunisia). *Tectonophysics*, *176*(1), 229–243. https://doi.org/10.1016/0040-1951(90)90268-D

Neri, G., Orecchio, B., Totaro, C., Falcone, G., & Presti, D. (2009). Subduction beneath southern Italy close the ending: Results from seismic tomography. *Seismological Research Letters*, *80*(1), 63–70. https://doi.org/10.1785/gssrl.80.1.63

Orecchio, B., Presti, D., Totaro, C., Guerra, I., & Neri, G. (2011). Imaging the velocity structure of the Calabrian arc region (southern Italy) through the integration of different seismological data. *Bollettino di Geofisica Teorica ed Applicata*, *52*(4).

Paige, C. C., & Saunders, M. A. (1982). Lsqr: An algorithm for sparse linear equations and sparse least squares. *ACM Transactions on Mathematical Software*, *8*(1), 43–71. https://doi.org/10.1145/355984.355989

Palano, M. (2014). On the present-day crustal stress, strain-rate fields and mantle anisotropy pattern of Italy. *Geophysical Journal International*, *200*(2), 969–985. https://doi.org/10.1093/gji/ggu451

Palano, M., Ursino, A., Spampinato, S., Sparacino, F., Polonia, A., & Gasperini, L. (2020). Crustal deformation, active tectonics and seismic potential in the Sicily channel (central Mediterranean), along the nubia–eurasia plate boundary. *Scientific Reports*, *10*(1), 1–14. https://doi.org/10.1038/s41598-020-78063-1

Panza, G., Pontevivo, A., Chimera, G., Raykova, R., & Aoudia, A. (2003). The lithosphere-asthenosphere: Italy and surroundings. *Episodes*, *26*(3), 169–174. https://doi.org/10.18814/epiiugs/2003/v26i3/003

Parello, F., Allard, P., D'Alessandro, W., Federico, C., Jean-Baptiste, P., & Catani, O. (2000). Isotope geochemistry of Pantelleria volcanic fluids, Sicily Channel rift: A mantle volatile end-member for volcanism in southern Europe. *Earth and Planetary Science Letters*, *180*(3–4), 325–339. https://doi.org/10.1016/s0012-821x(00)00183-7

Piana Agostinetti, N., & Amato, A. (2009). Moho depth and Vp/Vs ratio in peninsular Italy from teleseismic receiver functions. *Journal of Geophysical Research*, *114*(B6), B06303. https://doi.org/10.1029/2008JB005899

Piromallo, C., Becker, T. W., Funiciello, F., & Faccenna, C. (2006). Three-dimensional instantaneous mantle flow induced by subduction. *Geophysical Research Letters*, *33*(8), L08304. https://doi.org/10.1029/2005GL025390

Piromallo, C., & Morelli, A. (1997). Imaging the Mediterranean upper mantle by *P*-wave travel time tomography. *Annals of Geophysics*, *40*(4). https://doi.org/10.4401/ag-3890

Piromallo, C., & Morelli, A. (2003). *P* wave tomography of the mantle under the Alpine-Mediterranean area. *Journal of Geophysical Research*, *108*(B2). https://doi.org/10.1029/2002JB001757

Plomerová, J., Kouba, D., & Babuška, V. (2002). Mapping the lithosphere–asthenosphere boundary through changes in surface-wave anisotropy. *Tectonophysics*, *358*(1), 175–185. https://doi.org/10.1016/S0040-1951(02)00423-7

Pondrelli, S. (2002). European-Mediterranean regional centroid-moment Tensors catalog (RCMT) [Data set]. Istituto Nazionale di Geofisica e Vulcanologia. https://doi.org/10.13127/rcmt/euromed

Pondrelli, S., Morelli, A., Ekström, G., Mazza, S., Boschi, E., & Dziewonski, A. (2002). European-Mediterranean regional centroid-moment tensors: 1997–2000. *Physics of the Earth and Planetary Interiors*, *130*(1), 71–101. https://doi.org/10.1016/s0031-9201(01)00312-0

Pontevivo, A., & Panza, G. (2002). Group velocity tomography and regionalization in Italy and bordering areas. *Physics of the Earth and Planetary Interiors*, *134*(1), 1–15. https://doi.org/10.1016/S0031-9201(02)00079-1

Prada, M., Ranero, C., Sallares, V., Grevemeyer, I., de Franco, R., Gervasi, A., & Zitellini, N. (2020). The structure of Mediterranean arcs: New insights from the Calabrian arc subduction system. *Earth and Planetary Science Letters*, *548*, 116480. https://doi.org/10.1016/j.epsl.2020.116480

Prada, M., Sallares, V., Ranero, C., Vendrell, M., Grevemeyer, I., Zitellini, N., & de Franco, R. (2015). The complex 3-D transition from continental crust to backarc magmatism and exhumed mantle in the Central Tyrrhenian basin. *Geophysical Journal International*, *203*(1), 63–78. https://doi.org/10.1093/gji/ggv271

Presti, D., Billi, A., Orecchio, B., Totaro, C., Faccenna, C., & Neri, G. (2013). Earthquake focal mechanisms, seismogenic stress, and seismotectonics of the Calabrian arc, Italy. *Tectonophysics*, *602*, 153–175. https://doi.org/10.1016/j.tecto.2013.01.030

Rawlinson, N., Fichtner, A., Sambridge, M., & Young, M. K. (2014). *Chapter one - Seismic tomography and the assessment of uncertainty*. In R. Dmowska (Ed.), (Vol. 55, p. 1–76). Elsevier. https://doi.org/10.1016/bs.agph.2014.08.001

Reuther, C.-D., Ben-Avraham, Z., & Grasso, M. (1993). Origin and role of major strike-slip transfers during plate collision in the central Mediterranean. *Terra Nova*, *5*(3), 249–257. https://doi.org/10.1111/j.1365-3121.1993.tb00256.x

Sadeghisorkhani, H., Gudmundsson, Ó., & Tryggvason, A. (2018). GSpecDisp: A matlab GUI package for phase-velocity dispersion measurements from ambient-noise correlations. *Computers & Geosciences*, *110*, 41–53. https://doi.org/10.1016/j.cageo.2017.09.006

Sambridge, M. (1999a). Geophysical inversion with a neighbourhood algorithm—I. Searching a parameter space. *Geophysical Journal International*, *138*(2), 479–494. https://doi.org/10.1046/j.1365-246X.1999.00876.x

Sambridge, M. (1999b). Geophysical inversion with a neighbourhood algorithm—II. Appraising the ensemble. *Geophysical Journal International*, *138*(3), 727–746. https://doi.org/10.1046/j.1365-246x.1999.00900.x

Scarfì, L., Barberi, G., Barreca, G., Cannavò, F., Koulakov, I., & Patanè, D. (2018). Slab narrowing in the Central Mediterranean: The Calabro-Ionian subduction zone as imaged by high resolution seismic tomography. *Scientific Reports*, *8*(1), 1–12. https://doi.org/10.1038/s41598-018-23543-8

Serpelloni, E., Anzidei, M., Baldi, P., Casula, G., & Galvani, A. (2005). Crustal velocity and strain-rate fields in Italy and surrounding regions: New results from the analysis of permanent and non-permanent GPS networks. *Geophysical Journal International*, *161*(3), 861–880. https://doi.org/10.1111/j.1365-246x.2005.02618.x

Serpelloni, E., Faccenna, C., Spada, G., Dong, D., & Williams, S. D. P. (2013). Vertical GPS ground motion rates in the Euro-Mediterranean region: New evidence of velocity gradients at different spatial scales along the nubia-eurasia plate boundary. *Journal of Geophysical Research*, *118*(11), 6003–6024. https://doi.org/10.1002/2013JB010102

Sgroi, T., Barberi, G., & Marchetti, A. (2021). The contribution of the NEMO-SN1 seafloor observatory to improve the seismic locations in the Ionian Sea (Italy). *Annals of Geophysics*, *64*(6), SE655. https://doi.org/10.4401/ag-8575

Sgroi, T., Polonia, A., Barberi, G., Billi, A., & Gasperini, L. (2021). New seismological data from the Calabrian arc reveal arc-orthogonal extension across the subduction zone. *Scientific Reports*, *11*(1), 473. https://doi.org/10.1038/s41598-020-79719-8

Shapiro, N. M., Ritzwoller, M. H., Molnar, P., & Levin, V. (2004). Thinning and flow of Tibetan crust constrained by seismic anisotropy. *Science*, *305*(5681), 233–236. https://doi.org/10.1126/science.1098276

Spakman, W. (1990). Tomographic images of the upper mantle below central Europe and the Mediterranean. *Terra Nova*, *2*(6), 542–553. https://doi.org/10.1111/j.1365-3121.1990.tb00119.x

Spakman, W., van der Lee, S., & van der Hilst, R. (1993). Travel-time tomography of the European-Mediterranean mantle down to 1400 km. *Physics of the Earth and Planetary Interiors*, *79*(1), 3–74. https://doi.org/10.1016/0031-9201(93)90142-V

Tatsumi, Y. (1986). Formation of the volcanic front in subduction zones. *Geophysical Research Letters*, *13*(8), 717–720. https://doi.org/10.1029/GL013i008p00717

Totaro, C., Koulakov, I., Orecchio, B., & Presti, D. (2014). Detailed crustal structure in the area of the southern Apennines-Calabrian arc border from local earthquake tomography. *The Journal of Geology*, *82*, 87–97. https://doi.org/10.1016/j.jog.2014.07.004

Trippetta, F., Petricca, P., Billi, A., Collettini, C., Cuffaro, M., Lombardi, A. M., et al. (2019). From mapped faults to fault-length earthquake magnitude (FLEM): A test on Italy with methodological implications. *Solid Earth*, *10*(5), 1555–1579. https://doi.org/10.5194/se-10-1555-2019

Trua, T., Serri, G., & Marani, M. P. (2003). Lateral flow of African mantle below the nearby Tyrrhenian plate: Geochemical evidence. *Terra Nova*, *15*(6), 433–440. https://doi.org/10.1046/j.1365-3121.2003.00509.x

van der Lee, S., Deschamps, A., Margheriti, L., & giardini, D. (1999). *Midsea - mantle investigation of the deep suture between Eurasia and Africa*. International Federation of Digital Seismograph Networks. https://doi.org/10.7914/SN/YF_1999

van der Meijde, M., van der Lee, S., & Giardini, D. (2003). Crustal structure beneath broad-band seismic stations in the Mediterranean region. *Geophysical Journal International*, *152*(3), 729–739. https://doi.org/10.1046/j.1365-246X.2003.01871.x

Vedova, B., Lucazeau, F., Pasquale, V., Pellis, G., & Verdoya, M. (1995). Heat flow in the tectonic provinces crossed by the southern segment of the European geotraverse. *Tectonophysics*, *244*(1), 57–74. https://doi.org/10.1016/0040-1951(94)00217-W

Vozar, J., Jones, A. G., Fullea, J., Agius, M. R., Lebedev, S., Le Pape, F., & Wei, W. (2014). Integrated geophysical-petrological modeling of lithosphere-asthenosphere boundary in central Tibet using electromagnetic and seismic data. *Geochemistry, Geophysics, Geosystems*, *15*(10), 3965–3988. https://doi.org/10.1002/2014GC005365

Wathelet, M. (2008). An improved neighborhood algorithm: Parameter conditions and dynamic scaling. *Geophysical Research Letters*, *35*(9), L09301. https://doi.org/10.1029/2008GL033256

Wathelet, M., Chatelain, J.-L., Cornou, C., Giulio, G. D., Guillier, B., Ohrnberger, M., & Savvaidis, A. (2020). Geopsy: A user-friendly open-source tool set for ambient vibration processing. *Seismological Research Letters*, *91*(3), 1878–1889. https://doi.org/10.1785/0220190360

Wathelet, M., Jongmans, D., & Ohrnberger, M. (2004). Surface-wave inversion using a direct search algorithm and its application to ambient vibration measurements. *Near Surface Geophysics*, *2*(4), 211–221. https://doi.org/10.3997/1873-0604.2004018

Weidle, C., Soomro, R. A., Cristiano, L., & Meier, T. (2013). Identification of response and timing issues at permanent European broadband stations from automated data analysis. *Advances in Geosciences*, *36*, 21–25. https://doi.org/10.5194/adgeo-36-21-2013

Weiss, T., Siegesmund, S., Rabbel, W., Bohlen, T., & Pohl, M. (1999). Seismic velocities and anisotropy of the lower continental crust: A review. In D. Gajewski & W. Rabbel (Eds.), *Seismic exploration of the deep continental crust: Methods and concepts of DEKORP and accompanying projects* (pp. 97–122). Birkhäuser Basel. https://doi.org/10.1007/978-3-0348-8670-3_6

Wessel, P., Luis, J. F., Uieda, L., Scharroo, R., Wobbe, F., Smith, W. H. F., & Tian, D. (2019). The Generic Mapping Tools version 6. *Geochemistry, Geophysics, Geosystems*, *20*(11), 5556–5564. https://doi.org/10.1029/2019GC008515

West, M., Ni, J., Baldridge, W. S., Wilson, D., Aster, R., Gao, W., & Grand, S. (2004). Crust and upper mantle shear wave structure of the southwest United States: Implications for rifting and support for high elevation. *Journal of Geophysical Research*, *109*(B3), B03309. https://doi.org/10.1029/2003JB002575

Yang, Y., & Ritzwoller, M. H. (2008). Characteristics of ambient seismic noise as a source for surface wave tomography. *Geochemistry, Geophysics, Geosystems*, *9*(2). https://doi.org/10.1029/2007GC001814

Yang, Z., & Chen, W.-P. (2010). Earthquakes along the East African Rift system: A multiscale, system-wide perspective. *Journal of Geophysical Research*, *115*(B12), B12309. https://doi.org/10.1029/2009JB006779

Yogodzinski, G. M., Lees, J. M., Churikova, T. G., Dorendorf, F., Wöerner, G., & Volynets, O. N. (2001). Geochemical evidence for the melting of subducting oceanic lithosphere at plate edges. *Nature*, *409*(6819), 500–504. https://doi.org/10.1038/35054039

Zhang, S., & Karato, S.-I. (1995). Lattice preferred orientation of olivine aggregates deformed in simple shear. *Nature*, *375*(6534), 774–777. https://doi.org/10.1038/375774a0

Zhou, Y., Ni, S., Chu, R., & Yao, H. (2016). Accuracy of the water column approximation in numerically simulating propagation of teleseismic PP waves and Rayleigh waves. *Geophysical Journal International*, *206*(2), 1315–1326. https://doi.org/10.1093/gji/ggw212

Zhu, H., Bozdağ, E., & Tromp, J. (2015). Seismic structure of the European upper mantle based on adjoint tomography. *Geophysical Journal International*, *201*(1), 18–52. https://doi.org/10.1093/gji/ggu492

References From the Supporting Information

Boschi, L., Weemstra, C., Verbeke, J., Ekström, G., Zunino, A., & Giardini, D. (2012). On measuring surface wave phase velocity from station–station cross-correlation of ambient signal. *Geophysical Journal International*, *192*(1), 346–358. https://doi.org/10.1093/gji/ggs023